Journal of Structural Geology 179 (2024) 105035

Contents lists available at ScienceDirect

Journal of Structural Geology

journal homepage: www.elsevier.com/locate/jsg

Structural control on the alteration and fluid flow in the lithocap of the Allumiere-Tolfa epithermal system

Barbara Marchesini [a,b,*], Stefano Tavani [b,c], Marco Mercuri [a], Nicola Mondillo [c], Mattia Pizzati [d], Fabrizio Balsamo [d], Luca Aldega [a], Eugenio Carminati [a]

[a] Dipartimento di Scienze della Terra, Sapienza Università di Roma, Roma, Italy
[b] Consiglio Nazionale delle Ricerche, IGAG, Roma, Italy
[c] Dipartimento di Scienze della Terra, dell'Ambiente e delle Risorse, Università degli Studi di Napoli Federico II, Italy
[d] Dipartimento di Scienze Chimiche, della Vita e della Sostenibilità Ambientale, Università di Parma, Italy

ARTICLE INFO

Keywords:
Fracturing
Fluid-rock interaction
Argillization
Epithermal systems

ABSTRACT

Zones of advanced argillic alteration with general low permeability (i.e., lithocaps) are common place in the shallow parts of porphyry and epithermal ore deposits and active geothermal systems. The study of structural control on alteration distributions is of paramount importance for exploitation purposes as it really influences the caprock efficiency. We present the results of a structural-mineralogical study carried out in the lithocap of the Allumiere-Tolfa epithermal system (Northern Apennines). We characterized the composition, textures and physical properties (i.e., *in-situ* permeability; relative rock strength) of alteration facies. We then integrated field structural analysis with analysis of a virtual outcrop model to reconstruct the geometry of principal fluid-corridors. It resulted that advanced argillic alteration was promoted by circulation of highly reactive fluid(s) along a complex network of NE- and NW-striking faults and fractures dissecting the acidic volcanic dome. Such structures likely developed in response to a local disturbance of the regional stress field due to the extrusion of the Tolfa dome, which controlled the syn-extensional mineralization of the Allumiere-Tolfa area.

1. Introduction

In many active geothermal systems, porphyry and epithermal ore deposits, argillization is a very important shallow alteration process responsible for the formation of extensive (up to tens of square kilometers) superficial bodies of altered- and well zoned rocks with very-low permeability (e.g., Sillitoe et al., 1998; Krupp and Seward, 1987; Maza et al., 2021; González-Partida et al., 2022). Argillization in acidic geothermal environments may thus promote the formation of efficient caprocks above the reservoir, limiting the upward movements of hot convective currents and thus guaranteeing, below it, high pressure and temperature conditions necessary for the exploitation of geothermal energy (e.g., Barbier, 2002). The characterization of the tectonic evolution, reactivation history and permeability of caprocks is thus crucial to evaluate its seal efficiency. Most of the literature on geothermal exploration is focused on the characterization and modeling of the reservoir (e.g., Erkan et al., 2008; Ganguly and Mohan Kumar, 2012; Vignaroli et al., 2013; Brogi et al., 2016; Giordano et al., 2016; Salinas et al., 2021), whereas studies regarding characterization of caprocks are still limited (e.g., Corrado et al., 2014; Carapezza et al., 2015; Maffucci et al., 2016; Amanda et al., 2022; Hu et al., 2023).

Fault and fractures modulate fluid circulation in the crust, behaving either as preferential pathways for fluid migration or hydraulic barriers, or can switch from one behaviour to the other during fault activity and tectonic history (e.g., Caine et al., 1996). Infiltration of highly reactive fluids along faults facilitates alteration of the chemical-mineralogical and physical properties of pristine rocks along the alteration front and promotes the formation of ore deposits (e.g., Luhmann et al., 2017; Macente et al., 2017; Masoch et al., 2022; Rossetti et al., 2011; Luo et al., 2015; Zucchi et al., 2022). Crucial mechanisms controlling permeability in the alteration front of hydro- and geo-thermal systems include: 1) dissolution of host rock-forming minerals, 2) element mobility and 3) precipitation of new mineral phases as secondary minerals along structural discontinuities (i.e., fault and fractures) and in pores (e.g., Sibson 1987; Wintsch et al., 1995; Rossetti et al., 2011; Balsamo et al., 2013; Smith et al., 2013; Williams et al., 2017; Marchesini et al., 2022; Masoch et al., 2022). These mechanisms promote a complex distribution of altered rocks with extremely variable mechanical behavior along the

* Corresponding author. Dipartimento di Scienze della Terra, Sapienza Università di Roma, Roma, Italy.
E-mail address: barbara.marchesini@uniroma1.it (B. Marchesini).

https://doi.org/10.1016/j.jsg.2023.105035
Received 12 April 2023; Received in revised form 4 December 2023; Accepted 7 December 2023
Available online 15 December 2023

alteration front and, potentially, a heterogeneous permeability.

The study of exhumed hydrothermal systems and their comparison with analogue active geothermal systems is a quite recent approach on geothermal studies (e.g., Liotta et al., 2021). This comparison is extremely useful to understand the relationships between structures and fluid circulation of areas under exploration, with benefit in the de-risking of failed drillings.

To contribute to this topic, we present a structural-mineralogical and mechanical characterization of the lithocap of the Allumiere-Tolfa epithermal system belonging to the Tuscany-Latium geothermal region in the Northern Apennines, which was widely explored for geothermal energy since the beginning of the XX century (e.g., Cataldi et al., 1969, 1978; Duchi et al., 1992; Batini et al., 2003; Gianelli et al., 1997; Doveri et al., 2010; Chiodini et al., 2007; Chiarabba et al., 1995; Taussi et al., 2022). The lithocap is exposed in an abandoned quarry nearby the Allumiere village. The quarry dimensions (nearly 60 m high and 250 m wide), the easy accessibility, and the continuity of outcrops provide an outstanding opportunity for a multiscale structural and mineralogical study. We combine geological field mapping, analysis of digital outcrop model, structural and microstructural analyses, X-ray diffraction (XRD), and measurements of *in-situ* permeability and relative rock strength of alteration products to unravel the structural and permeability evolution of the lithocap. Thus, we were able to reconstruct the evolution of the Allumiere-Tolfa lithocap from a tectonic, mineralogical and rheological point of view, proposing an evolutionary model that can be applied to other geothermal systems characterized by alteration of volcanic rocks (see Browne, 1978; Moeck, 2014 for reviews and Yang et al., 2001; Agostini et al., 2006, Vázquez et al., 2014 and for specific case studies worldwide).

2. Geological setting

2.1. Regional geology - The Northern Apennines

The Northern Apennines (Fig. 1a) is part of the Apennine chain, an arc-shaped, NE-verging fold-and-thrust belt, which originated in the framework of the convergence between the Adria microplate and the European margin. The belt is an accretionary prism developed along the W-directed subduction of the Alpine Tethyan oceanic realm, followed by the subduction of the continental lithosphere of the Adria microplate, underneath the Sardinia-Corsica continental block belonging to the European margin (Carminati and Doglioni, 2012). In the last stages, subduction was possibly substituted by lithospheric delamination (Faccenda et al., 2009; Zhang et al., 2022). In the Northern Apennines and in the study area, this process led to the overthrusting of oceanic rocks (i.e., Ligurian domain) on top of the distal portion of the Adria passive margin (Tuscan and Umbria-Marche sedimentary successions; Conti et al., 2020). Owing to slab retreat, compression in the Apenninic wedge migrated towards E-NE, as witnessed by the age of the foredeep deposits (Middle Miocene to present from the inner Northern Apennines to the present-day Adriatic Sea foredeep; Ricci Lucchi, 1986) and by radiometric constraints on thrust activity (Curzi et al., 2022). Slab retreat also determined the opening of the Tyrrhenian backarc basin, leading to crustal thinning and the development of post-orogenic extensional faults that rejuvenate towards the NE (Cavinato and Celles, 1999). Extensional tectonics, associated with a NE-SW tensile stress field, was roughly synchronous with subduction-related magmatism (Peccerillo, 2005; Carminati and Doglioni, 2012) that led to the development of several ore deposits (e.g., Brogi et al., 2011; Rossetti et al., 2011; Zucchi et al., 2022) and geothermal systems (e.g., Barberi et al., 1984; Barberi et al., 1994; Batini et al., 2003; Vignaroli et al., 2013).

2.2. The allumiere-tolfa area

The study area follows the evolution of the Northern Apennines belt, being characterized by thrusting of a deep water Upper Cretaceous-Oligocene calcareous sedimentary succession (locally named Tolfa Flysch) of Ligurian affinity (i.e., the sedimentary cover of the Tethys Ocean; Fig. 1c) on top of Mesozoic marine carbonates of the Tuscan domain (Fazzini and MP, 1972, Fig. 1c).

The Tolfa flysch belongs to the Ligurian Units (e.g., Marroni et al., 2001) of the orogenic wedge and it is characterized by alternating calcarenites, limestones, marly carbonates and shales (Funiciello et al., 2012). Following Fazzini and MP (1972), the Tolfa Flysch lithotypes exposed in the study area are, from bottom to top: Argillaceous-calcareous flysch Fm., Calcareous Flysch I Fm., Mignone Fm., Calcareous Flysch II Fm., Arenaceous Flysch Fm. (see Funiciello et al., 2012; for further details).

The Tolfa Flysch Unit is tectonically overlain by the Pietraforte Unit (Fig. 1c), not exposed in the area of Fig. 2a, which is characterized by Upper Cretaceous marls at the bottom evolving to siliciclastic turbidites towards the top (Funiciello et al., 2012).

Sandy conglomerates and clayey marine sediments with evaporitic horizons were unconformably deposited on top of these allochthonous Units during the late Miocene extensional stage (Fig. 1c).

The area was later uplifted and domed by the intrusion of an acidic pluton within the sedimentary succession, associated with the activity of the Tolfa-Cerite volcanic district. K-Ar dating ascribes the extrusion of domes to 3.5 Ma (Villa et al., 1989). In the Tolfa area, magmatic products were likely extruded along a major NE-SW-striking fault (Tolfa fault) developed during back-arc extension (de Rita et al., 1997, Fig. 2).

The geometry of the magmatic bodies and their geometrical relationship with the surrounding sediments suggest that magma has been extruded as cryptodomes, broadly in the shape of a laccolith, causing the general uplift of the area (De Rita et al., 1997; Cimarelli and de Rita, 2006, Fig. 2c). Although volcanic rocks of the Tolfa area bear a strong imprint of late hydrothermal acid sulfate alteration, chemical and petrological characterization of less altered rocks indicate a silicic composition between trachydacitic and rhyodacyte (Pinarelli 1991; de Rita et al., 1997) and are traditionally included into the Tuscan magmatic province (Poli et al., 2003).

In the study area, Pleistocene tuffs belonging to the nearby Sabatini Volcanic District are outcropping in the eastern sector (Fig. 2a) but they were not considered in the present study.

2.3. Hydrothermal mineralization in the allumiere-tolfa area

The study area has been affected by post volcanic hydrothermal activity, which gave rise to a wide abundance of mineral resources, which have been intensively exploited since the Middle Ages until the last century (Della Ventura and Patanè, 2020). In particular, the hydrothermal activity produced two distinct mineralized areas. The first area is located south of the Allumiere village, within the sedimentary country rocks, and is mainly characterized by Fe-oxide and metal (Pb, Fe, Cu, Zn, Ag, Hg)-sulfide mineralization (Ferrill et al., 2021; Calderoni et al., 1985, Fig. 2b). The second area is located to the north of the Allumiere village and prevailingly has alunite and kaolinite deposits, related to alteration of the volcanic rocks. The Allumiere quarry is the biggest ore alunite and kaolinite deposit located in the second area (Fig. 2a).

3. Methods

The studied outcrop is located in a quarry nearly 60 m high and 250 m wide (Fig. 3a), organized into 5 benches. We used a multiscale structural, petrographic and mineralogical approach to characterize the chemical alteration in the exposed lithocap and to reconstruct its evolutionary history. Firstly, we have built a high-resolution 3D model of the quarry, using original digital images collected by an unmanned aerial vehicle (UAV) and processed using the Structure from Motion Multiview Stereo photogrammetric pipeline. The 3D model allowed us to map the major faults and the distribution of alteration facies and to

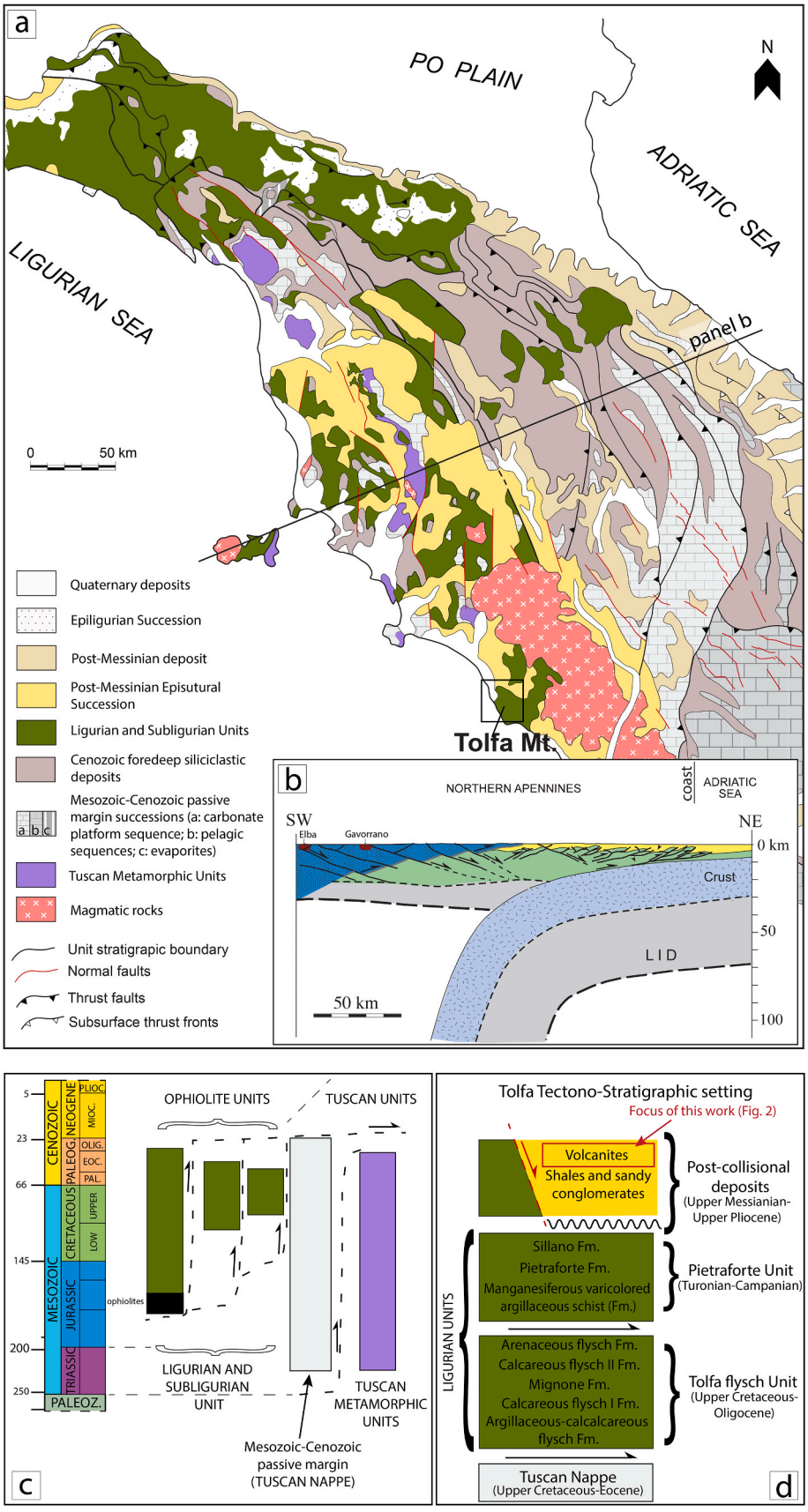

(caption on next page)

Fig. 1. Geological framework of the study area. (a) Simplified geological map of the Northern Apennines (Italy) showing the main thrusts, faults, principal tectonic units and location of the study area. Modified after (Cerrina Feroni et al., 2004)and (Conti et al., 2020). (b) Schematic crustal cross-section through the Northern Apennines (modified after (Carminati and Doglioni, 2012)showing the Tyrrhenian backarc rift associated with the Apennines subduction. (c) Tectono-stratigraphic relationship among the different tectonic units of Northern Apennines and related paleogeographical domains (modified after (Brogi et al., 2005)). (d) Tectono-stratigraphic setting of the Tolfa area, showing the main tectonic relation between the fourth main Tectonic Units.

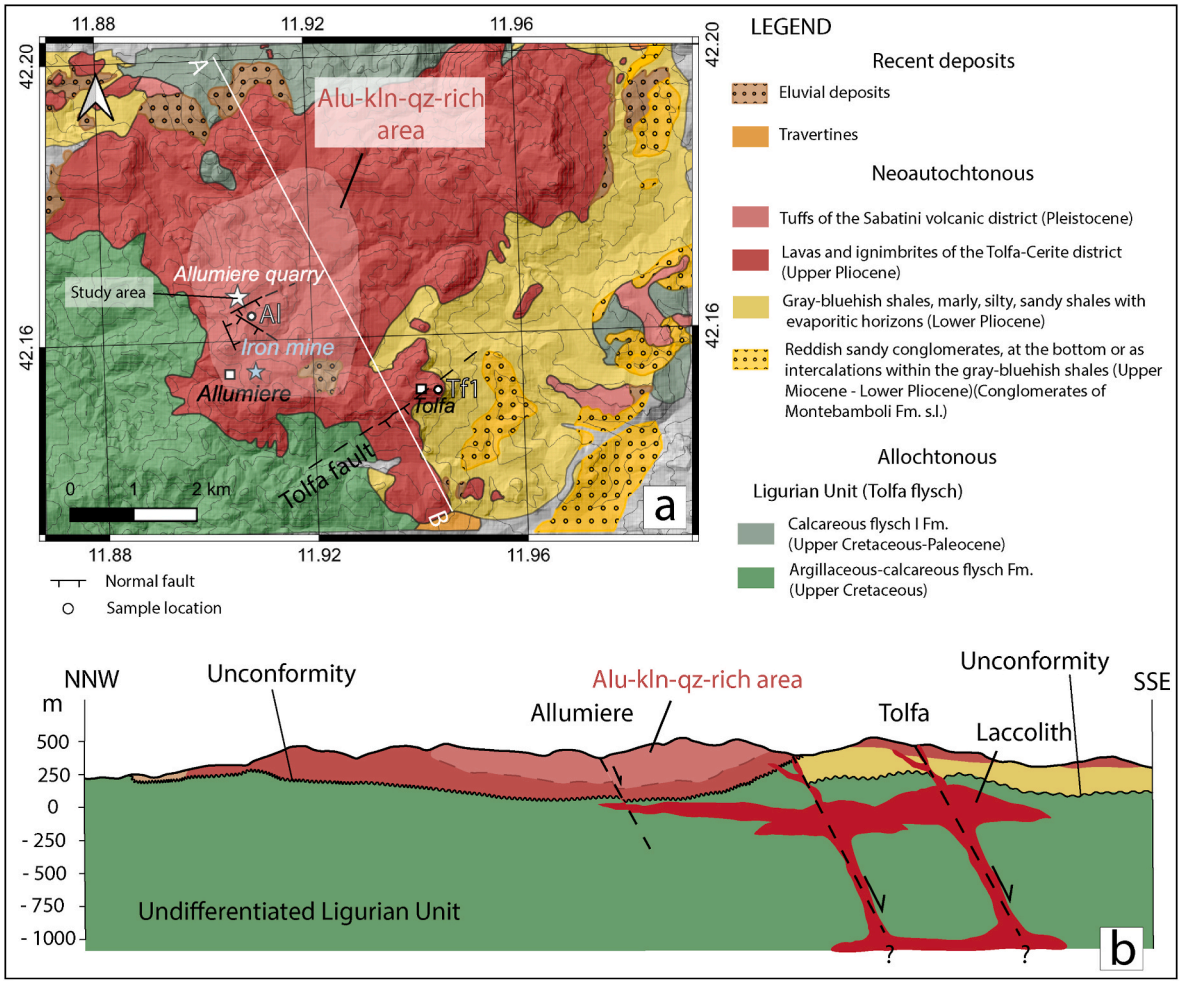

Fig. 2. (a) Simplified geological map of the Allumiere -Tolfa area, presenting the outcropping lithologies in the proximal area of interest (after Fazzini et al. (1972). Location of the Tolfa fault is drawn after de Rita et al. (1997). The location of the Allumiere quarry is marked by the white star. Light blue star indicates the major Iron Mine in the study area. (c) Schematic cross-section of the study area (after Fazzini et al., 1972; de Rita et al., 1997; Cinti et al. 2011). Deep structures below the dotted area are interpreted.

gather structural (i.e., faults, veins, joints) and mineralogical data into a single 3D environment (Fig. 3). Locations of structural data are reported in Fig. S1 in the Supplementary Material. Chemical characterization of the exposed rocks has been firstly performed by *in-situ*-XRF (XRF data expressed in oxides are reported in Table S2). We then integrated these preliminary data with XRD analysis and petrographic investigations on thin sections (optical microscopy and SEM-EDS analysis). Sample locations are reported in Fig. 3a whereas the list of samples is reported in Table S1. For various altered lithotypes, *in-situ* permeability and uniaxial compressive strength measurements were determined using an air–mini-permeameter and a Schmidt hammer, respectively. The recognized lithotypes were then mapped in the Allumiere quarry by integrating the above-mentioned data with field surveying and interpretation of the 3D model. The analytical methods are thoroughly described in the Supplementary Material.

4. Results

On the basis of field observations, whole-rock composition and microstructural analysis, we recognized three main alteration facies typical of epithermal mineralizations, which, following the classical scheme of Hedenquist et al. (2000), can be classified as (a) the residual quartz facies, (b) the advanced argillic facies (i.e., quartz-alunite-kaolinite) and (c) the argillic or intermediate argillic facies (i.e. containing smectite to illite-smectite halo in less altered country rock; Fig. 3). However, some local complexities on mineral association linked to supergene alteration and on macrostructures have been recognized and reported in the map presented in Fig. S2.

Rocks belonging to the residual quartz facies are located in the inner portion of the quarry and are arranged as five distinct cores with a dome shape of variable length and width (up to 200 m × 70 m; Fig. 3a).

Rocks of the advanced argillic alteration facies occur as 150–170 m wide band, roughly oriented NW-SE, embedding the silicified cores (Fig. 3a). Locally, relicts of bedding planes of the original volcanic rock

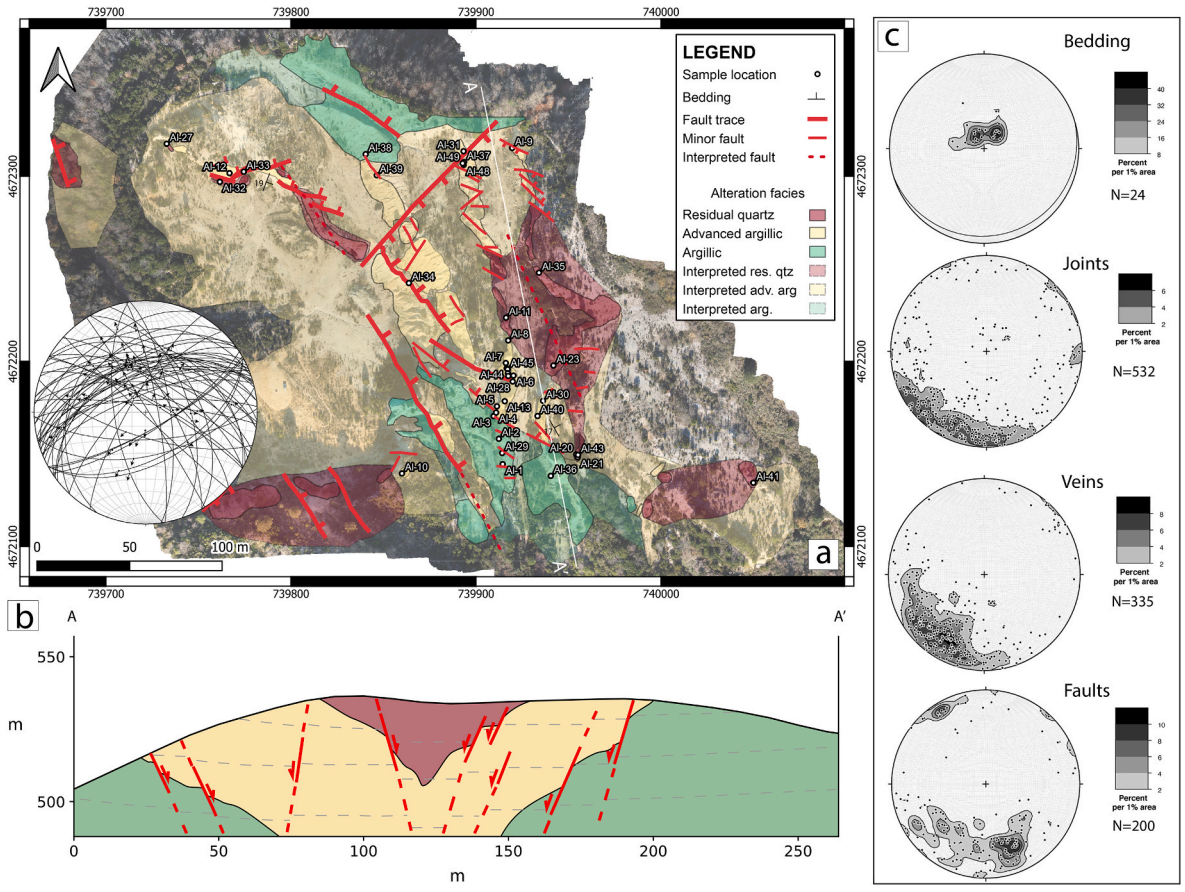

Fig. 3. Geological-structural map and geological cross section of the Allumiere quarry (see Fig. 2a for location). (a) Distribution of exposed alteration facies and main faults and fractures mapped in the field. Base map is an aerial orthoimage obtained from the virtual outcrop model. The chosen color scale indicates a progressive increase in the alteration degree from distal areas (green) towards internal areas (red) of the quarry. The Schmidt net (lower hemisphere projection) of attitudes of measured faults related kinematic indicators (slickenfibers). (b) Schematic cross-section of the alteration geometry. (c) The Schmidt nets showing the attitudes of bedding, joints, veins and faults. Bedding occurs as relict flow-banding of the pristine volcanic deposits.

are still recognizable, showing sub-horizontal attitude (Fig. 3c).

Argillic alteration facies crops out in distal parts of the quarry at the outer boundary of the advanced argillic alteration facies volumes, and occurs in 100–120 m wide bands with NW-SE orientation (Fig. 3a).

The meso- and micro-structural and mineralogical characters of the alteration facies are described in the following sections, together with the main features of the unaltered protolith.

4.1. *Petrography and mineralogy of the protolith*

We collected a representative sample of the unaltered protolith at the Tolfa village (sample: Tf1; Fig. 2a; Table S1), in the proximity of the Madonna della Rocca Sanctuary.

X-ray diffraction analysis of the bulk composition shows that sample Tf1 contains K-feldspar (48%), plagioclase (42%), and biotite (10%) with traces of clinopyroxene and tridymite. The X-ray pattern also shows broad humps at low diffraction angles (6° and 12.1 °2θ) suggesting the incipient formation of smectite and halloysite respectively at the expense of volcanic glass (e.g., Aldega et al., 2009). This mineral assemblage is consistent with a volcanic rock of trachitic composition in agreement with previous works in the area (Negretti, 1962; de Rita et al., 1997; Cimarelli and de Rita 2006).

Petrographic analysis shows that the volcanic host rock has a porphyritic texture, characterized by coarse grains (500 μm - 1 mm thick) phenocrystals embedded in a finer ipocrystalline matrix (Fig. 4a). Phenocrystals are plagioclase and K-feldspar showing Carlsbad twinning (Fig. 4c), biotite (Fig. 4c) and minor pyroxene (Fig. 4d), locally altered (Fig. 4c). Locally, feldspars are cross-cut by secondary sealed fractures, marked by fluid inclusion trails (Fig. 4d).

4.2. *Argillic alteration facies*

At the mesoscale, the argillic alteration facies is characterized by poorly consolidated rocks with yellowish-ocher color (Fig. 5a) made of K-feldspar (51–84%), quartz (12–30%), kaolinite (2–8%), with variable amounts of smectite (Table 1; Fig. 5c–e). The presence of K-feldspar is associated with discrete amounts of K_2O detected through *in-situ* XRF analysis (Table S2). Crystals of the volcanic host rock are still recognizable in the field, despite being characterized by variable degrees of hydrothermal alteration (Fig. 5b).

Microstructural analysis shows distinct millimeter-thick pseudomorphic grains, deriving from the variable alteration of former phenocrysts, embedded in a microcrystalline matrix of quartz and feldspars (Fig. 5d–f). Specifically, we observed residual unaltered K-feldspar phenocrysts (Fig. 5d), kaolinite pseudomorphs after completely altered K-feldspars (Fig. 5f), and smectite pseudomorphs after plagioclase (Fig. 5d–e). Svanbergite has been locally observed in association with smectite (Fig. 5e). Svanbergite shows a microcrystalline pseudocubic texture and forms small aggregates (20–30 μm; Fig. 5e).

4.3. *Advanced argillic (quartz-alunite-kaolinite) alteration facies*

At the mesoscale, the quartz-alunite-kaolinite alteration facies consists of whitish rocks with soapy appearance (typical of kaolinite-alunite

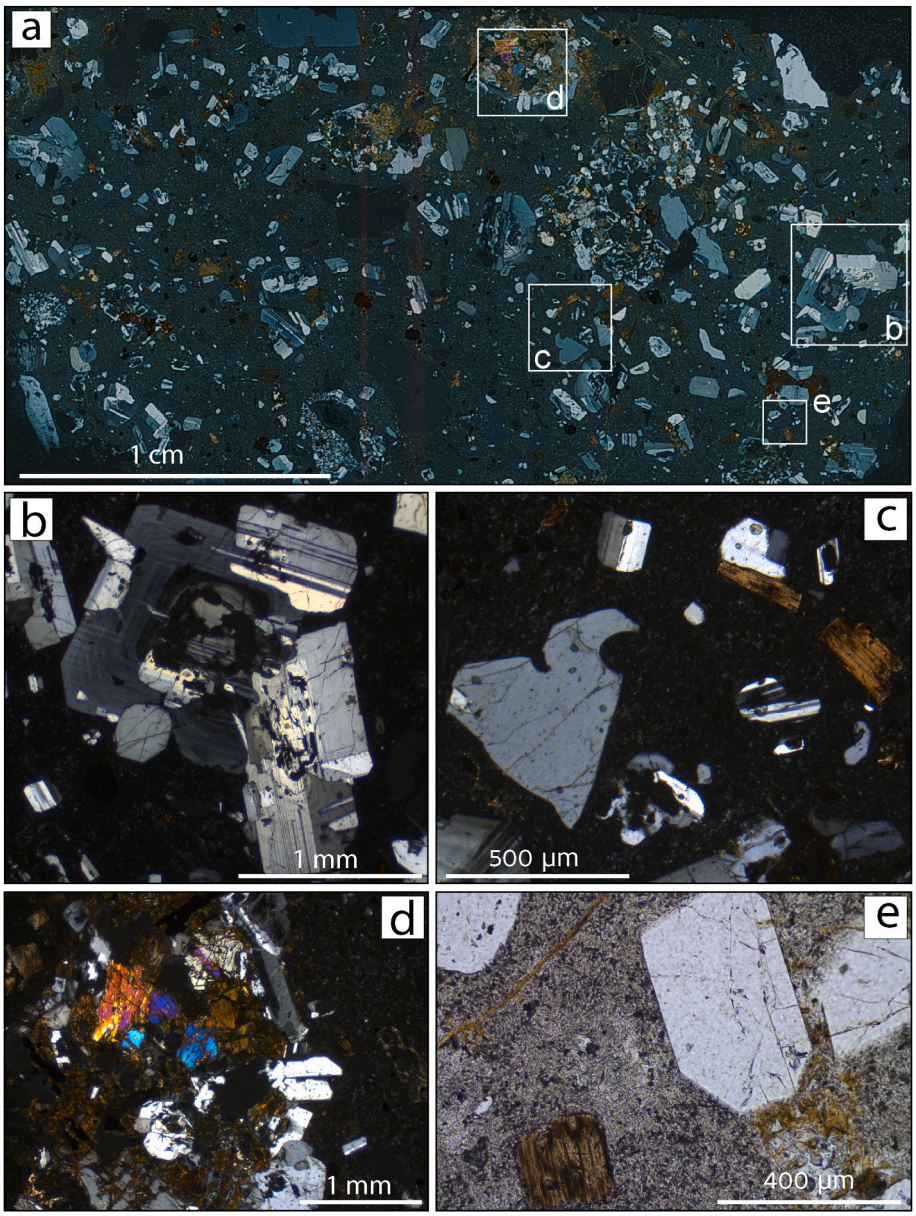

Fig. 4. Petrographic analysis of the unaltered volcanic rock (Sample Tf1). (a) Photomicrograph (cross polarized light) of the thin section. The rock is made of phenocrysts of (b) millimeter-thick plagioclase and zoned K-feldspar, (c) prismatic crystals of K-feldspar showing Carlsbad twinning, biotite and minor (d) pyroxene, (e) embedded in a fine volcanic matrix.

mineralization) that are more competent than those of the argillic facies (Fig. 6a). The quartz-alunite-kaolinite rocks are widely crosscut by numerous generations of alunite-kaolinite-rich veins of variable thickness (between 4 cm and 30 cm; Fig. 6a). Locally, some alunite-kaolinite veins show a silicified halo (Al-44; Al-45).

The quartz-kaolinite-alunite facies is characterized by quartz (26–55%), alunite (2–18%), natroalunite (1–24%), kaolinite (28–74%), dickite (2–3%). Anatase, gorceixite, barite and smectite occur as trace amounts (Table 1; Fig. 6b). Occasionally, cristobalite and halloysite have also been identified (Table 1). The presence of alunite and kaolinite corresponds to high amounts of SO_3 and Al_2O_3 in the rocks (field XRF data; Table S2).

At the microscale, this facies is characterized by heterogeneous texture with aggregates of kaolinite crystals forming pseudomorphs after K-feldspar and microcrystalline aggregates of alunite embedded in vacuolar silica (Fig. 6c–d). Kaolinite occurs in distinct crystals with hexagonal texture and grain size between 20 and 50 μm (Fig. 6e–f).

Alunite, referred as Alu1 hereafter, fills the vugs in the form of crystalline aggregates or geodes (Fig. 6e), has a platy texture with grain size between 20 and 50 μm and is zoned to natroalunite, with natroalunite at the nucleus (Fig. 6d).

Boundaries between residual quartz facies and advanced argillic facies is transitional and it is characterized by centimetric-to-metric isolated blocks of strongly silicified blocks embedded in a fine and low-competent matrix with yellowish-whitish appearance (Fig. 6g). Veins and fractures pervasively cross-cut the quartz-alunite-kaolinite-rich matrix (Fig. 6g). We performed XRD analysis on both the isolated blocks and the matrix. The blocks are characterized by quartz (2–92%), cristobalite (35–93%), alunite (2–3%), kaolinite (1–41%), pyrite (1–4%) and traces of anatase and natroalunite (Table 1; Fig. S3). The matrix is instead characterized by quartz (1–73%), cristobalite (2–93%), tridymite (3–24%), alunite (1–89%), kaolinite (1–68%), halloysite (2–5%), pyrite (1%), gorceixite (1%), goethite (1%), anatase (1%) and traces of K-feldspar and fluorencite (Table 1; Fig. S3). Occasionally dickite,

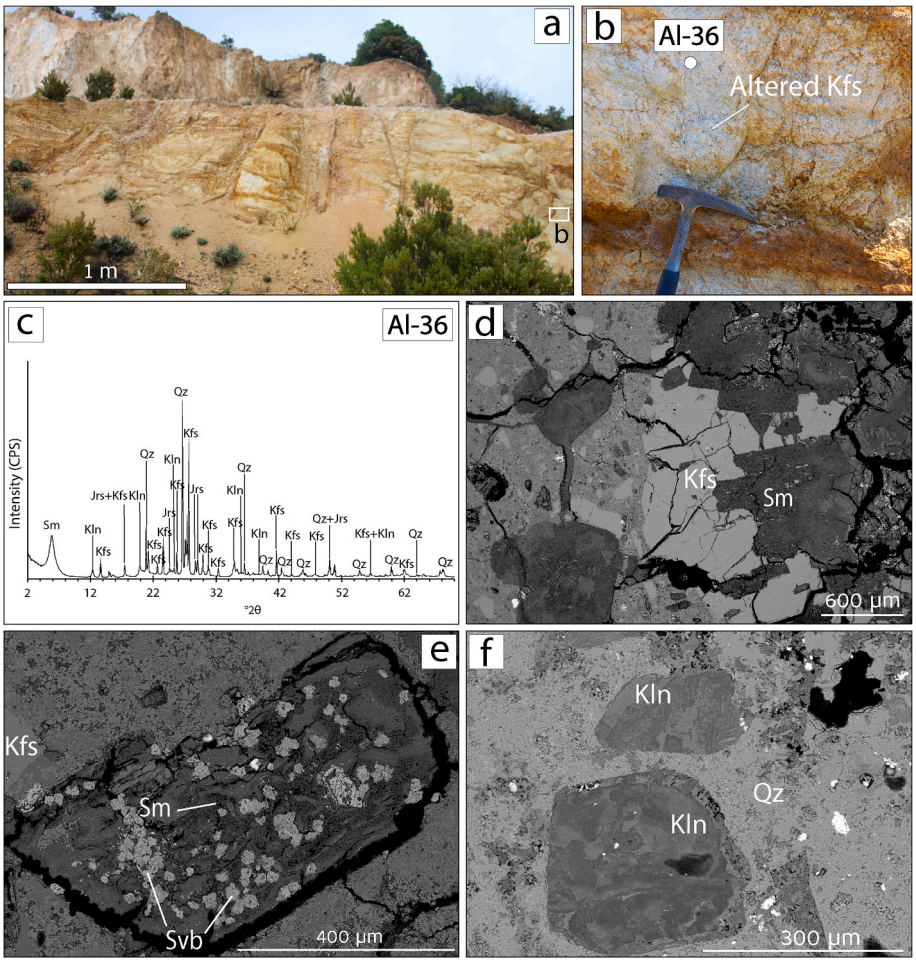

Fig. 5. Meso- and microscale characterization of the argillic alteration facies. (a) At the mesoscale the argillic alteration facies appears as a poorly consolidated yellowish material with a low-to-moderate degree of alteration of the pristine volcanic rock. (b) Rocks are characterized by an aphanitic texture with millimetric-thick phenocrysts mainly of K-feldspar embedded in a fine matrix. K-feldspar crystals are extensively altered. (c) XRD pattern of a representative sample of the argillic alteration facies (sample Al-36) showing the occurrence of kaolinite (Kln), K-feldspar (Kfs), quartz (qz), jarosite (Jrs) and smectite (Sm). At the microscale, this facies is texturally characterized by (d) subhedral residual K-feldspar phenocrystals embedded in a microcrystalline matrix of quartz and K-feldspar. Former plagioclase crystals are replaced by (e) smectite and minor svanbergite (sample Al-29; Table S1). (f) Kaolinite is formed by replacing K-feldspar (sample Al-36).

dolomite, halite and zircon have also been observed (Table 1).

4.4. Residual quartz facies

At the mesoscale the residual quartz facies consists of massive-brownish rocks with very high competence (Fig. 7a). Locally, the residual quartz facies is characterized by pockets with a vuggy texture (Fig. 7a), with alunite partially filling vugs (Fig. 7b). Vugs have diameters of a few millimeters (Fig. 7b). Alunite-kaolinite-rich veins locally cross-cut the residual quartz facies (Fig. 7a).

The residual quartz facies consists of quartz recrystallized from residual silica, as suggested by the high content of cristobalite (59%), quartz (8%), and tridymite (see e.g. Hedenquist and Arribas, 2022). Other minerals are alunite (24%), natroalunite (5%), kaolinite (2%), and gorceixite (2%; Table 1; Fig. 7c).

Microstructural analysis shows that the vugs are partially filled by Alu1 crystals (Fig. 7d). In addition, it appears that the silica matrix contains disseminated cubic pyrite crystals of grain size between 5 μm and 25 μm (Fig. 7e). Pyrite is locally As-bearing.

4.5. Supergene alteration

Both at the mesoscale and at the microscale it is evident a diffuse supergene alteration overprinting locally the aforementioned facies. The supergene alteration is characterized by widespread Fe-oxy-hydroxides (also confirmed by high amounts of Fe_2O_3 detected by XRF analyses; Table S2), which occur as surficial coatings or pseudomorphs after pyrite in association with silicified rocks (Fig. 8a), and jarosite. The pseudomorphic goethite shows a typical supergene texture characterized by internal concretions (Fig. 8a–b) and contains inclusions of cinnabar (HgS; Fig. 8c).

In the supergene assemblage, it was identified a second generation of alunite filling veins and cavities, here named Alu2. Alu2 crystals are characterized by cubic texture and grain size between 10 μm and 30 μm (Fig. 8a). As-Fe-hydroxides (e.g., symplesite) arranged along intergranular pores are associated with Alu2 (Fig. 8b).

4.6. Structural pattern and fault zone architecture

The alteration zoning is pervasively affected by faults, veins and joints (Fig. 3). Faults are organized in two major systems, with extensional kinematics, striking NE-SW and NW-SE, respectively (Fig. 3a, c). The evaluation of the lateral extent of these main faults outside the quarry is unfortunately hindered by anthropic activities and thick vegetation. Locally, minor faults with displacements of a few centimeters also show a strike-slip component (Fig. 3a). Moreover, the quarry is widely cross-cut by joints that are more abundant in the residual quartz facies exposed in the upper part and lower part of the quarry wall

Table 1
X-ray semiquantitative analysis of matrix samples. Interpreted alteration facies is indicated for each sample.

Sample	Whole-rock composition (%wt.)																	Zrc	Trace minerals	Alteration facies
	Qz	Crs	Trd	Kfs	Alu	Na-alu	Kln	Dck	Jrs	Hal	Sm	Py	Hl	Gor	Gth	Ant	Dol	Sd		
Al-1	12			84			2		2										Sm	Argillic
Al-2	20			74			5				1								Jrs	Argillic
Al-3	30			51			8		11										Sm	Argillic
Al-36	17			79			2		2		1								Sm	Argillic
Al-4	72						26						2						Na-alu, Goe	Advanced argillic
Al-5	37	2			7	2	49													Advanced argillic
Al-6	55					1	42						3			1			Brt	Advanced argillic
Al-7	1		3		89		1			5				1	1					Advanced argillic
Al-8	29				2		68					1							Ant	Advanced argillic
Al-9	55				2	11	28	3						1	1				Jrs	Advanced argillic
Al-10	26	2			4	24	41	2						1	1					Advanced argillic
Al-11	8	59			24	5	2							2						Residual quartz
Al-13	46				18	1	32						2				1		Gor	Advanced argillic
Al-20	23		20		8		45					1				1	3			Advanced argillic
Al-28	22	35			2		41													Advanced argillic
All-34	1				4	14	74			4						2		1	Hem, Dol, Sm, Gth	Advanced argillic
Al-37	18	11			10	56								2	5		2	1	Ant	Advanced argillic
Al-38	66				21	8	2	15		2				1					Kfs	Advanced argillic
Al-46	50	2					44						1		1	1		1	Fluorencite	Advanced argillic
Al-35	2	93					1					4							Alu, Na-alu	Residual quartz
Al-21	73		24		1		2									1				Residual quartz
Al-27	92				3		4					1							Ant, Dol	Residual quartz

Acronyms: Qz: quartz; kfs: K-feldspar; alu: alunite; kln: kaolinite; jrs: jarosite; na-alu: natroalunite; hl: halite; crs: cristobalite; py: pyrite; gor: gorceixite; hem: hematite; sm: smectite; wm: white micas; dol: dolomite; brt: baryte; mm: montmorillonite; dck: dickite; ant: anatase; gth: goethite; sd: siderite; hall: halloysite (tubular kaolinite); brt: baryte; smc: smectite; tridymite: trd; sm: smythite; sd:siderite; zrc: zircon.

(Fig. 3). On the contrary, veins are more abundant in the advanced argillic and argillic facies (Fig. 6).

Both joints and veins are mostly near vertical and perpendicular to bedding (Fig. 3). Cumulative contouring of joints and veins poles shows similar spreading of strike between N-S and E-W directions, with an average NW-SE orientation (Fig. 3).

Faults are characterized by a complex architecture, in which structures are frequently hidden by chemical alteration (Fig. 9). Fault zones are formed by sharp contacts with striation and well-developed damage zones or, in case of more complex interaction between faulting and alteration, they are marked by strongly silicified centimetric-to-metric isolated blocks embedded in a fine and low-competent matrix with yellowish-whitish appearance.

Although displacement of major faults cannot be accurately measured due to the lack of reliable pre-kinematic markers and/or abrupt alteration facies boundaries, it can be bracketed between some m to few tens of m by the juxtaposition of different alteration facies (Figs. 3 and 9). Displacement is accommodated along single (Fig. 9b) or multiple (Fig. 9c) principal slip surfaces (PSS), which, in some cases, preserve striated slickensides (Fig. 9d). Locally, PSSs display “nastrino” bands, marked by a reddish 20–30 cm high surface (Fig. 9e) made mainly of kaolinite (74%), alunite (4%) and natroalunite (14%; sample Al-34; Table 1). At the microscale, we identified that the nastrino band is formed by one or more principal slip zones (PSZs) 400-500 μm-thick, which crosscut the kaolinite-dickite-rich matrix (Fig. 9f). The matrix also contains residual quartz/silica nuclei with resorbed boundaries. The PSZ is made of synkinematic Alu1, with crystal size of a few microns and platy texture (Fig. 9f). Alu1 is also locally zoned to natroalunite (Fig. 9f). Late goethite crystals also fill cavities within the PSZ (Fig. 9f). Intergrowth of svanbergite aggregates have also been observed in association with Alu1 in the PSZ, as well in association with kaolinite-rich veins (Table 1). Svanbergite shows a sub-euhedral texture and zoned texture (Fig. 9g).

X-ray diffraction analysis of fault gouge shows that it is made of alunite (28–35%), natroalunite (9–11%), kaolinite (16–37%), quartz (1–6%), cristobalite (16–36%; samples Al-48 and Al-49; Table 2).

4.7. Uniaxial compression strength and permeability along the principal alteration front

Distribution of the Q values (Fig. 10b) along the selected transect (Fig. 10a) shows that the mean Q value is very low (10–16%) for rocks belonging to the argillic facies, whereas it progressively increases (c. 48%) towards more quartz-rich areas, with a big jump at the transition between the advanced argillic alteration facies and residual quartz facies (samples: Al-7-Al-8; Fig. 10b). Conversely, *in-situ* permeability measurements show a reverse distribution of values with respect to uniaxial compression strength values with permeability decreasing from the argillic alteration facies towards the residual quartz facies (Fig. 10c). In particular, *in-situ* permeability varies between 982 mD and 133 mD in the argillic facies and between 14 mD and 0.03 mD in the residual quartz facies (Fig. 10c).

5. Discussion

Our multidisciplinary study allowed us to petrographically and structurally constrain the long-lasting alteration of the epithermal system in the Allumiere area. In particular, in the following paragraphs we discuss how NW-SE and NE-SW-oriented stretching occurred coevally with the rise of hydrothermal fluids and concomitant alteration of the volcanic rock to form the lithocap of the Allumiere-Tolfa epithermal system.

5.1. Genesis of alteration facies and fluid origin

The Allumiere quarry is characterized by a well-developed alteration

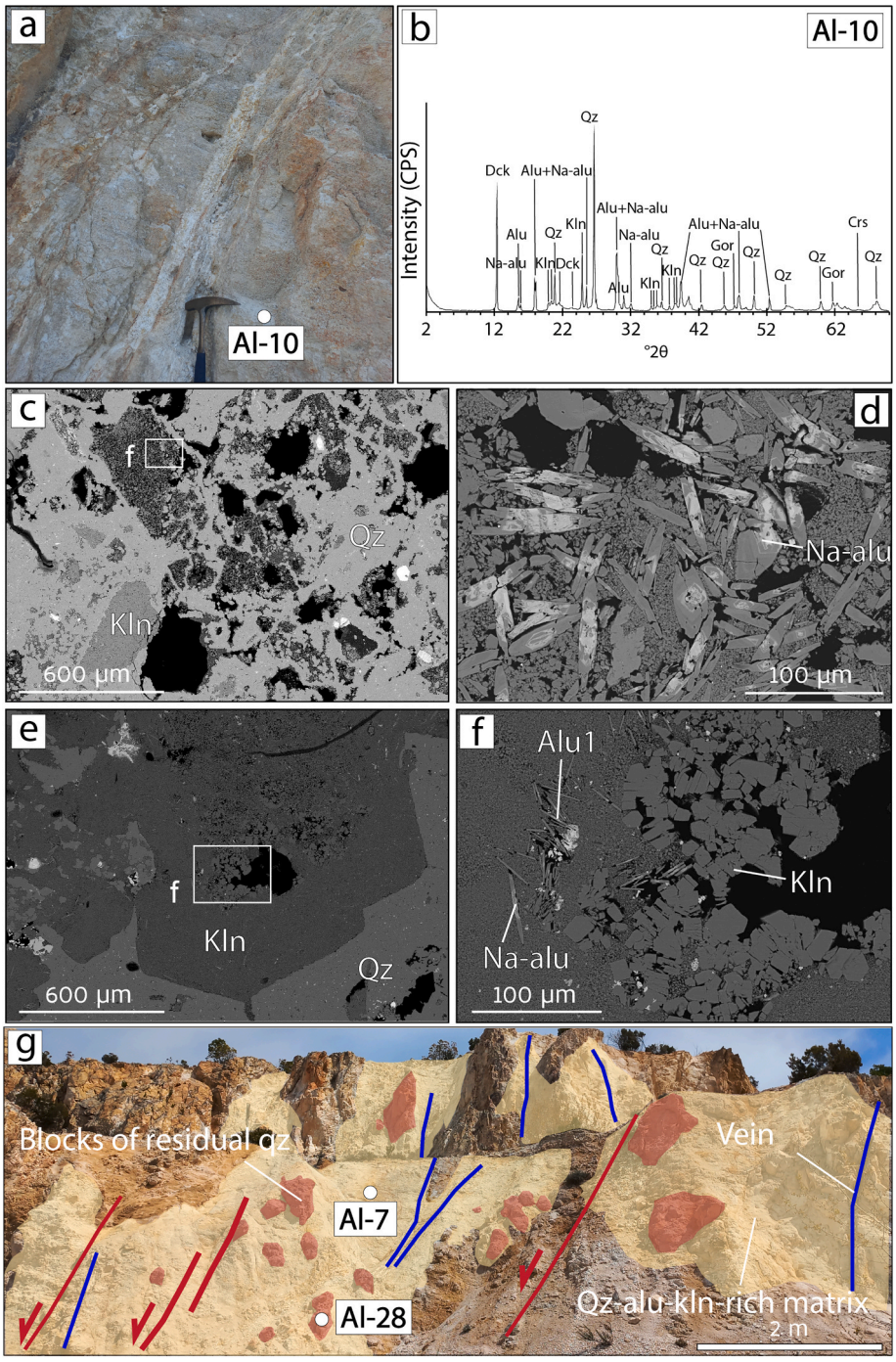

Fig. 6. Meso- and microstructural characterization of the advanced argillic quartz-alunite-kaolinite facies. (a) At the mesoscale this facies is characterized by whitish color and a soapy appearance. (b) Bulk mineralogy indicates the occurrence of quartz (Qz), alunite (Alu), natroalunite (Na-alu), kaolinite (Kln), cristobalite (Crs), dickite (Dck) and gorceixite (Gor). Panel (b) shows a representative XRD pattern of the quartz-alunite-kaolinite facies (sample: Al-10). At the microscale this facies is characterized by (c) vacuolar silica, associated with kaolinite and alunite, replacing the parent rock. (d) Alunite has a platy texture (Alu1). Alunite crystals are zoned to natroalunite, with natroalunite in the nuclei and alunite at the rims. (e) Kaolinite has a replacive pseudomorphic texture after K-feldspar, (f) partially acquiring a geodic feature in the nuclei of the pseudomorph. (g) Interpreted-field view of the boundary between residual quartz facies and advanced argillic facies. It is characterized by metric blocks of residual quartz embedded in a fine quartz-alunite-kaolinite matrix. Minor fractures and quartz-alunite-kaolinite-rich veins crosscut the advanced argillic facies.

zoning, where we identified three main alteration facies: 1) residual quartz facies; 2) advanced argillic facies; 3) argillic facies (Fig. 3). Each facies has a specific mineral assemblage (Table 1) and all of them are cross-cut by veins filled with various amounts of kaolinite and alunite.

The residual quartz facies occurs in various domes arranged in the central part of the quarry (Fig. 3), and it is characterized by a massive texture. It is made by quartz recrystallized from residual silica, as suggested by the large amounts of cristobalite and tridymite (Table 1; e.g., Hedenquist and Arribas, 2022). In this facies, vugs are mostly filled by sulphides and alunite (Fig. 7e–f; Table 1). Uniaxial compression strength and *in-situ* air-permeability measurements of the residual quartz facies indicate that these rocks are the stiffest rock types, with the lowest permeability (Fig. 10).

The silicified domes are surrounded by the advanced argillic facies

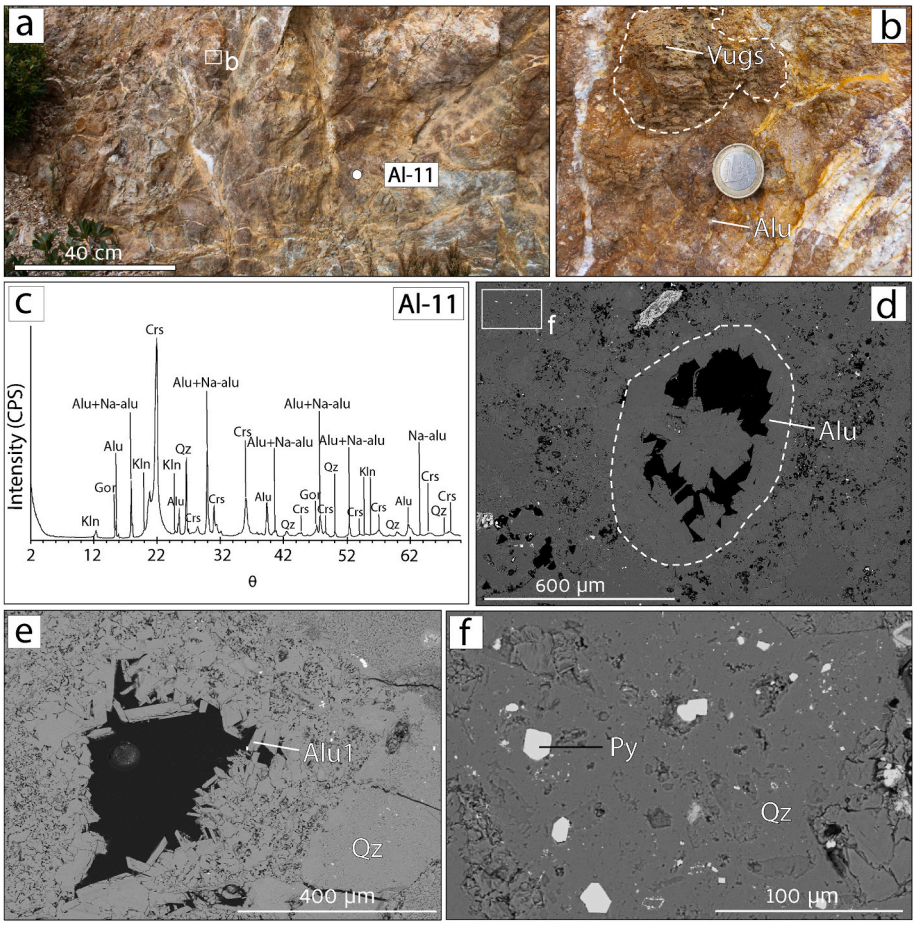

Fig. 7. Meso- and microstructural characterization of the residual quartz facies. (a) At the mesoscale this facies is characterized by strongly silicified rocks, widely cross cut by nearly vertical NW-SE-striking joints. (b) Strongly silicified rocks are characterized by blocks of residual quartz. Locally, it is characterized by vuggy texture, and by millimetric phenocrysts of alunite. (c) Representative XRD pattern for the residual quartz facies showing the occurrence of cristobalite (Crs), quartz (Qz), alunite (Alu), natroalunite (Na-alu), kaolinite (Kln), gorceixite (Gor; sample: Al-11). (d) At the microscale this facies is characterized by strongly silicified matrix and cavities filled by geodic alunite (e) with platy texture (Alu1; sample: Al-41). (f) Euhedral pyrite crystals fill intergranular pores in the silicified matrix (sample: Al-9).

(Fig. 3). Rocks of this facies are made of alunite-group (i.e., alunite, natroalunite, jarosite) and kaolinite-group (i.e., kaolinite, dickite, halloysite; Table 1) minerals and quartz. At the mesoscale, this facies is locally characterized by centimeter-to-meter sized blocks of residual quartz, embedded in a less cohesive and finer grained quartz-alunite-kaolinite-rich matrix (Fig. 6g). Uniaxial compression strength and *in-situ* air-permeability measurements of the advanced argillic facies are characterized by extremely heterogeneous mechanical strength and permeability values (Fig. 10). This is consistent with the variable mineral content (quartz amount varies between 1% and 72%; Table 1). The contact between the advanced argillic facies and the residual quartz facies is gradual and the transition zone is a few meters wide. Such a transitional zone is pervasively crosscut by veins and faults with displacement up to a few meters (Fig. 6g).

The argillic facies consists of relict of pristine K-feldspar, kaolinite, quartz and smectite, occurs in the outermost portions of the quarry and is never observed in direct contact with residual silica facies (Fig. 3).

Microstructural and textural analysis of rock samples from the three facies showed that the residual quartz facies, the advanced argillic facies and the argillic facies developed at the expense of primary minerals (K-feldspar, plagioclase, and biotite) and volcanic glass forming the volcanic protolith (Fig. 4). The altered facies identified in the Allumiere quarry represent the typical alteration phases produced by hydrolytic alteration of acidic-volcanic rocks due to circulation of acidic sulfate-rich fluid(s) (e.g., Hedenquist et al., 2000). This kind of alteration process is largely documented in the shallow portions of high-sulfidation epithermal deposits, forming an upward-flaring geometry of distinct alteration zones (i.e., Hedenquist et al., 2000). This is consistent with the geometry reconstructed for the Allumiere quarry (Fig. 3b). More in detail, the cross-section across the Allumiere quarry (Fig. 3b), shows that the residual quartz facies occupies the uppermost portion and it cannot be vertically connected with the main fluid conduit, likely occurring at depth. This is consistent with the interpretation that the exposed portion of the Allumiere-Tolfa epithermal system in the quarry corresponds to the lateral tip of the system.

Consistently with previous works in similar settings (e.g., Hedenquist et al., 2000), we infer that the circulation of acidic sulfate-rich fluid(s), with an initial pH of 1–2 and a temperature range between 160 °C and 270 °C (e.g., Hedenquist et al., 2000) promoted intense hydrolytic alteration of the host rock, and the formation of the three alteration facies documented in the Allumiere quarry. In particular, the high solubility of K and Al at pH < 2 (e.g., Ece et al., 2013) caused the complete alteration of the primary rock-forming minerals of pristine volcanics (i.e., K-feldspar, plagioclase, biotite). During this process SiO_2 remained as silica residue, with a local vuggy texture in the more altered zones (Fig. 7a–b), i.e., closer to the main fluid corridors. After the interaction within the residual quartz domes, the fluid was enriched in K and Al. At this stage the fluid pH gradually increased (i.e., pH comprised between 2 and 4; Hemley and Jones, 1964) causing the K-feldspar to be progressively altered to kaolinite-dickite and the contextual precipitation of

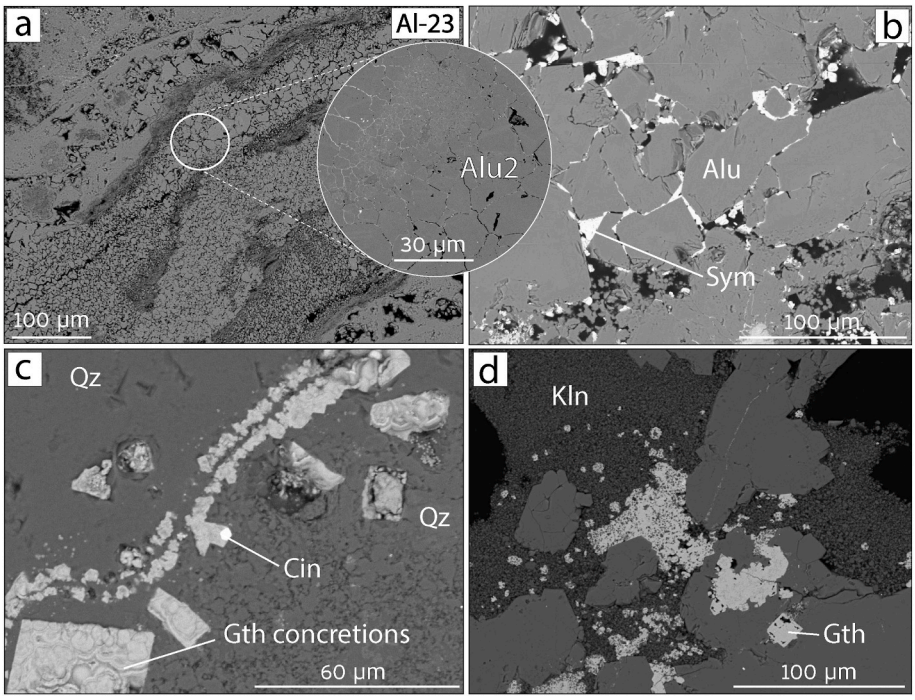

Fig. 8. Supergene alteration. (a) A second generation of alunite (Alu2) fills fractures crosscutting a quartz/silica-rich matrix. Alu2 is characterized by cubic crystals, 30 μm-thick, (sample: Al-23; Table S1). (b) As-Fe-hydroxides (e.g., symplesite) are arranged along Alu2 crystal edges, filling intergranular pores, in a vein. (c) and (d) Goethite pseudomorphs after pyrite, containing cinnabar (HgS) inclusions are found in the silicified host rock (sample: Al-43). Typical supergene goethite concretions are also identified.

alunite and natroalunite (Fig. 6). This process led to the formation of the advanced argillic facies. In more distal areas at pH > 2, under which Al tends to be insoluble, the argillic facies formed by replacement of K-feldspar with kaolinite crystals and by alteration of plagioclase to smectite (Inoue, 1995). Coevally with the above-described processes, enhanced circulation of K- and Al-rich fluids along fractures and fault zones, promoted the formation of the alunite- and kaolinite-rich veins.

The identified alteration assemblage is also consistent with the agate mineralizations identified c. 2–2.5 km away from the Allumiere quarry (Conte et al., 2022). This alteration mineral assemblage is typical of a fluid evolving from acidic to near-neutral pH conditions along the alteration front of lithocaps (e.g., Hedenquist and Arribas, 2022).

Regarding potential fluid origin, the occurrence of sulfates and sulphides, as documented in the Allumiere quarry, requires the external supply of a certain amount of S. In addition to sulfur of magmatic origin, geochemical analysis of fluid discharges and gas emissions performed in the western sector of the Sabatini Volcanic District and in the Tolfa Mountains, show that sulfate-rich fluid(s) are likely derived by interaction of hydrothermal fluids with the Triassic anhydrites occurring at depth in the Tuscan Unit and/or with the shallower evaporitic horizons associated with the Lower Pliocene sandy conglomerates (Cinti et al., 2011). Despite, our data do not allow us to choose a magmatic or an evaporitic origin (or a combination of the two) for sulfur, the presence of syn-kinematic alunite with platy texture (i.e., Alu1; Fig. 9f) in association with aluminum-phosphate-sulfate, such as svanbergite (Fig. 9g; Table 1), suggesting a deep fluid source (Rye et al., 1992; Ece and Schroeder 2007; Ece et al., 2013).

5.2. Structural pattern

Faults, joints and veins control and crosscut the various alteration facies indicating a syn-to post-alteration origin. Instead, with the exception of the volcanic layering, we have not recognized any centimeter-to meter-scale structures with a clear pre-alteration origin.

Faults, measured in the field (Fig. 3) and mapped in the quarry (Fig. 3a) are arranged into two mutually orthogonal systems, corresponding to NW-SE and NE-SW-striking structures. Measured striations indicate for both systems dominantly dip-slip extensional kinematics with subordinate right-lateral and left-lateral strike-slip components (Fig. 3a). These two extensional fault systems are recognized all along the Tyrrhenian margin of the Apennine chain and main volcanic fields are located at their intersection (Acocella and Funiciello 2006). At the regional scale, crustal thinning associated with the Tyrrhenian back-arc extensional opening was accommodated since the middle-late Miocene by both low- and high-angle normal faults (e.g., Jolivet et al., 1999; Collettini et al., 2006). This extensional system controlled the emplacement of magmatic bodies and the development of geothermal fields, such as the Monte Amiata geothermal field, (e.g., Rossetti et al., 2011; Acocella and Rossetti 2002; Brogi 2008; Dini et al., 2008). In the study area, the emplacement of the Tolfa Dome Complex (3.5 Ma; Villa et al., 1989) was structurally-controlled by a likely coeval NE-striking Pliocene master fault, i.e., the Tolfa fault, (de Rita et al., 1997; Cimarelli and de Rita, 2006). The occurrence of the two mutually perpendicular systems of extensional structures, one striking-perpendicular to the regional σ_3 and σ_2 stress axes, is the classical pattern in extensional settings (e.g., Ramsay and Huber, 1983; Engelder, 1987), occurring across multiple-scales (Gross, 1993; Destro, 1995; Bai et al., 2002; Ferrill et al., 2021). Accordingly, joints and veins in the Allumiere quarry should be organized into two distinct sets striking NE-SW and NW-SE. However, cumulative contouring of joint and vein poles shows a spread distribution with their strike ranging from N-S to E-W (Fig. 3). Such a spread distribution has been observed in extensional systems interacting with local sources of stress, such as diapirs and volcanic domes (e.g., Mège and Masson, 1996; Storti et al., 2011; Quintà et al., 2012; Maerten et al., 2022). In these dome-related environments, brittle fracturing is driven by a time-space evolving stress field, resulting from the competition between local (i.e., doming) and regional tectonic stress fields (e.g., Mège and Masson, 1996). Accordingly, we infer that jointing and veining in the Allumiere quarry provide a long-lasting record of the evolving stress field, and developed during the active rise of the Tolfa

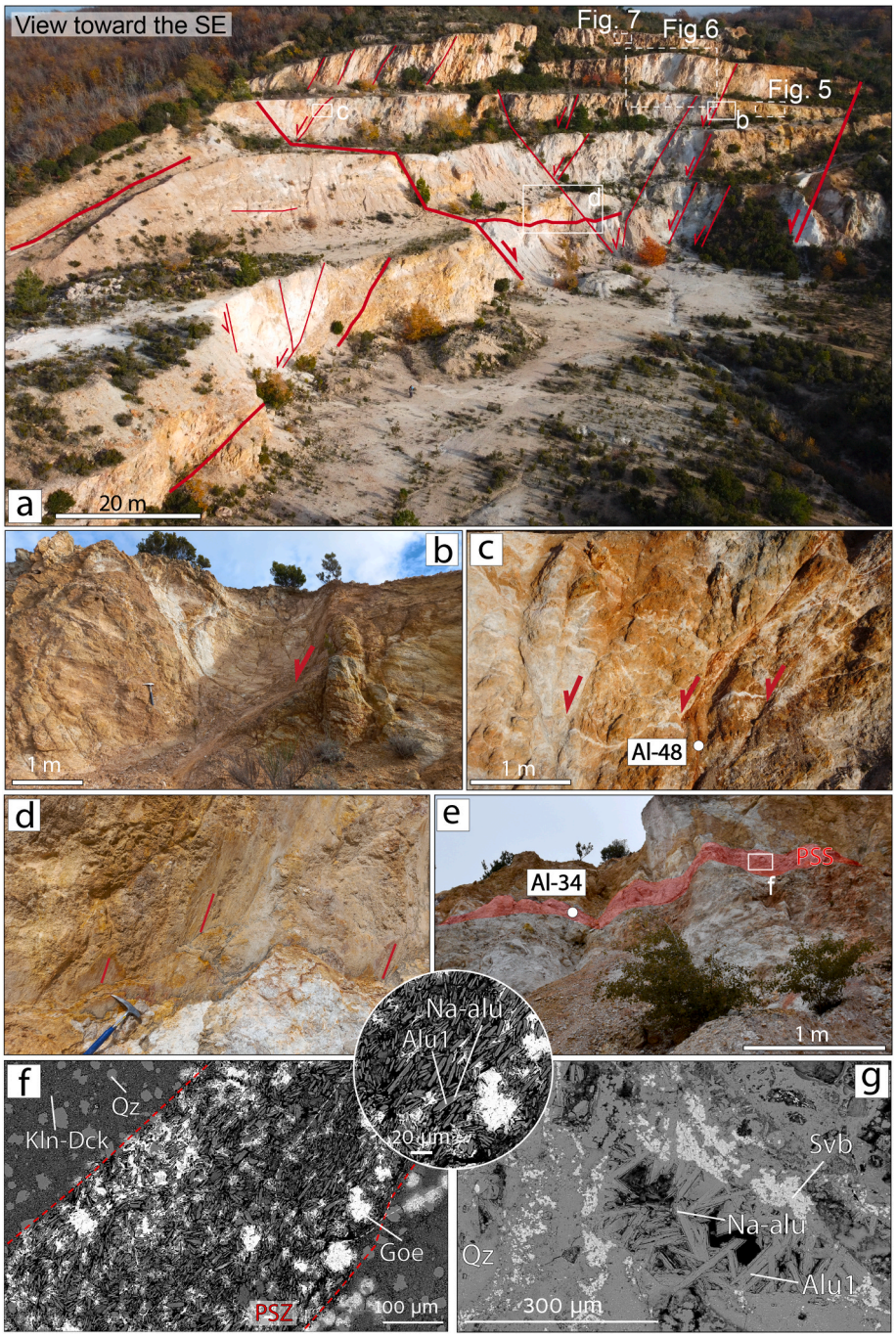

Fig. 9. Architecture of major fault zones and synkinematic mineralization. (a) Interpreted NW-SE view of the Allumiere quarry. Fault cores are characterized by (b) single or (c) multiple principal slip surfaces (PSSs). (d) Locally, PSSs are marked by freshly striated reddish nastrino bands, 15-20 cm thick. (e) At the microscale, PSSs are characterized by 400/500 μm-thick principal slip zones (PSZs) with synkinematic alunite-natroalunite mineralizations (Alu1). Late goethite crystals fill cavities within the PSZ. PSZ are crosscutting a kaolinite-rich host rock, which also contains residual quartz/silica nuclei with resorbed boundaries.

Dome Complex. On the other hand, meso-scale faults, which are well-clustered, did not record the overall evolution of the stress field, thus suggesting they developed in a shorter time lapse, likely at the beginning of doming.

5.3. *Inferred faults and evolution of the allumiere-tolfa epithermal system*

We propose the following tectonic-hydrothermal evolution for the Allumiere-Tolfa epithermal system: 1) crustal stretching led to the development of regional-scale NE-SW- and NW-SE-striking extensional faults and to the extrusion of the Tolfa Dome Complex; 2) Faulting and related fracturing above the Tolfa Dome enhanced the upwelling of hydrothermal fluids and consequent hydrolytic alteration of volcanic rocks; 3) Tectonically-controlled alteration produced the development of an upward-flaring geometry of distinct alteration zones. These alteration facies are roughly elongated in a NW-SE direction, suggesting a similar orientation for the alteration-controlling fault. Extensional deformation continued after hydrothermal alteration and resulted in the formation of NE-SW and NW-SE faults occurring at different scales in the Allumiere quarry. During the same extensional stage, jointing and veining developed, and continued during the late doming stage. We thus conclude that the Allumiere lithocap and its mineralization formed

Table 2
X-ray semiquantitative analysis of veins.

Sample	Whole-rock composition (%wt.)															Structure
	Qz	Crs	Alu	Na-alu	Kln	Dck	Hal	Sv	Py	Gor	Gth	Ant	Dol	Hem	Brt	Trace minerals	
Al-12	25		4	2	57	7								1	3	Gor	Kaolinite-oxyde/hydroxide vein
Al-39			65	30			1		1	3						Qz, Sm	Alunite vein
Al-40	1		3		96											Hl, Dol	Supergenic kln-alu vein
Al-44	5		3	7	81												Kaolinite-alunite vein
Al-45	81		1		17							1				Na-alu, Hl, Py	Silicified halo
Al-47	1	1			96			1			1						Kaolinite vein
Al-48	1	16	35	9	37								2				Fault gouge
Al-49	6	36	28	11	16								3				Fault gouge

Acronyms: Qz: quartz; kfs: K-feldspar; alu: alunite; kln: kaolinite; jrs: jarosite; na-alu: natroalunite; hl: halite; crs: cristobalite; py: pyrite; elb: elbaite; gor: gorceixite; hem: hematite; sm: smectite; wm: white micas; dol: dolomite; brt: baryte; mm: montmorillonite; dck: dickite; ant: anatase; gth: goethite; sd: siderite; hall: halloysite (tubular kaolinite); brt: baryte; smc: smectite; tridymite: trd; sm: smythite; sd:siderite.

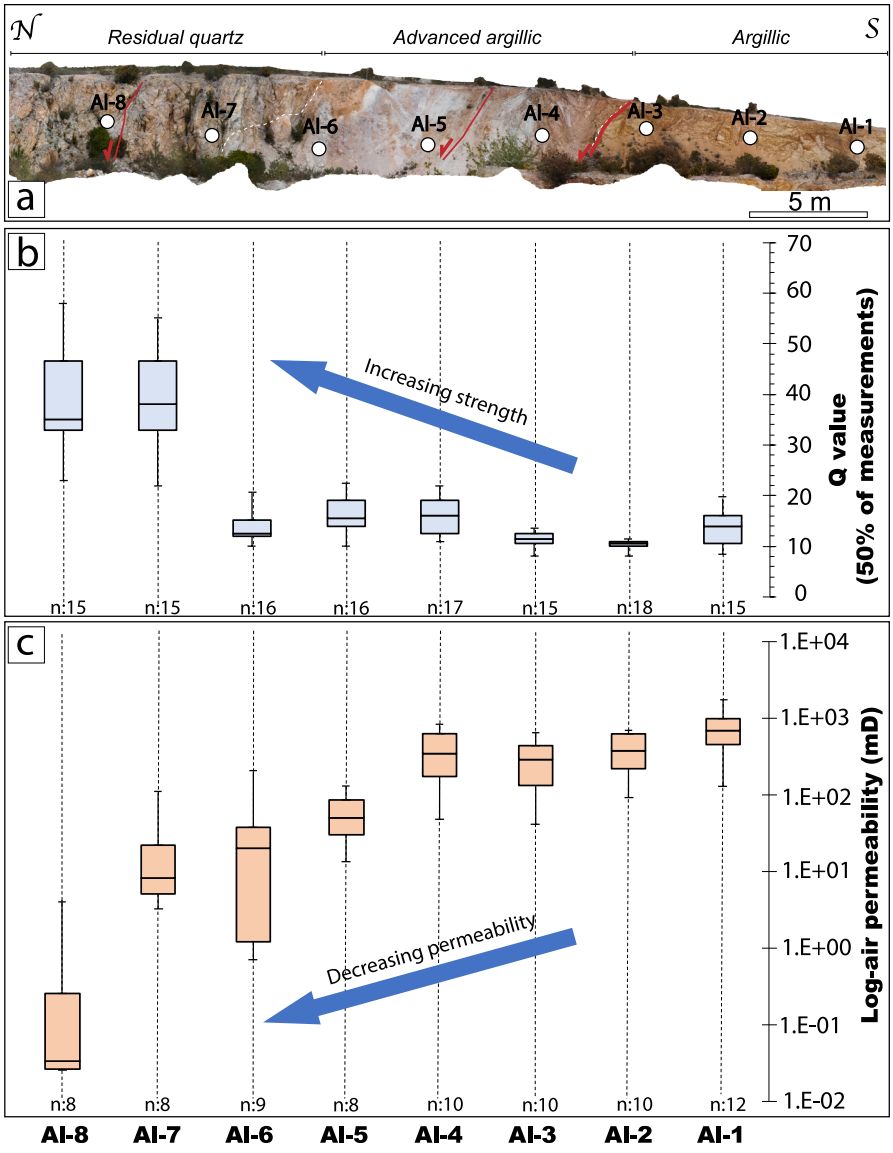

Fig. 10. Uniaxial compressive strength and in-situ air permeability measurements along a representative section of the principal alteration zoning. (a) Transect starts from the argillic facies (Al-1) towards the residual quartz facies (Al-8). (b) Schmidt hammer rock relative strength (Q value) measurements for different types of alteration facies along the transect. Lower limit of detection of Schmidt hammer is 8.5 Q. Each box of the box–and–whiskers plot represents the range between the 1st and 3rd quartile of the distribution. The whole data range is represented by the extension of the whiskers. Data show a progressive increase in strength towards silicified rocks (Al-8). (c) Logarithmic air-permeability (mD) value for each sampling site. Lower limit of the air-minipermeater is 0.01 mD. Each box of the box–and–whiskers plot represents the range between the 1st and 3rd quartile of the distribution. Data show a progressive decrease in permeability towards the silicified rocks. N, number of measurements for each structural area.

under an extensional regime. This is consistent with other works concerning the extensional-tectonic control on ore mineralizations in the Northern Apennines (e.g., Brogi et al., 2011; Liotta et al., 2021; Rossetti et al., 2011; Sillitoe et al., 1998). In particular, our study is in agreement with previous ones emphasizing the role of high-angle (both NE-SW and NW-SE-oriented) faults in favoring the rise of mineralizing fluids (e.g., Rossetti et al., 2011; Liotta et al., 2015). In the Allumiere case, the mineralization is principally controlled by a NW-SE-oriented fault, as evidenced by the elongation of alteration zoning, although we documented also the activity of both NE-SW- and NW-SE-striking faults coeval with the hydrothermal mineralization. Similar Pliocene and Quaternary NE-SW- and NW-SE-striking normal-to transtensional fault systems have been documented in both proximal active geothermal systems, i.e., Torre Alfina and Monte Amiata (e.g., Brogi 2008; Vignaroli et al., 2013) and exhumed fossil hydrothermal systems (e.g., Liotta et al., 2015) of the Tyrrhenian margin.

In terms of permeability evolution, we assume that the present-day permeability cannot be taken as representative of the initial permeability distribution, for which we can only draw some inferences. In particular, the NW-SE-elongation of alteration facies is coherent with a permeable damage zone linked to a NW-SE-striking fault favoring and controlling rise of hydrothermal fluids. Hydrolitic alteration promoted the formation of distinct lithostructural domains with different mechanical behavior and permeability. In particular, the formation of silica-rich domes along and above the main fluid corridors, likely enhanced fracturing and fluid circulation. In fact, reduction of matrix permeability in the residual quartz facies (Fig. 10) is accompanied by intense synkinematic jointing, which instead enhanced the fluid-carrier capacity of the faults (Smeraglia et al., 2021). The fracturing-related permeability enhancement in the silica-rich domains, coupled with the alteration-related permeability reduction within the advanced-argillic and argillic facies due to hydrolytic alteration process, promoted the formation of tectonically-controlled permeability domains, starting from a roughly homogeneously permeable pristine rock.

6. Conclusions

We present an integrated structural-mineralogical study on the lithocap of the Allumiere-Tolfa epithermal system. The present-day lithocap is the result of alteration of pristine volcanic rocks due to the upwelling of an acidic-sulfate-rich hydrothermal fluid. The distribution of the alteration facies is the final result of a tight interplay between faulting- and fracturing-related permeability evolution and fluid-rock interaction.

The evolution of the Allumiere-Tolfa epithermal system has occurred during the post-orogenic extension of the Tyrrhenian margin. In detail, extension triggered the rise of the Tolfa Dome. The upwelling of hydrothermal fluids was driven by a doming-related network of faults and fractures, which caused the pervasive alteration of pristine rocks into distinct alteration facies. Three genetic stages can be recognized: 1) crustal stretching led to development of regional-scale NE-SW- and NW-SE-striking extensional faults and to the extrusion of the Tolfa Dome. 2) Faulting and related fracturing above the Tolfa Dome enhanced the upwelling of hydrothermal fluids and consequent hydrolytic alteration of volcanic rocks. 3) Tectonically-controlled alteration produced the development of an upward-flaring geometry of distinct alteration zones, roughly striking-NW-SE.

We infer that jointing and veining in the Allumiere quarry are long-lasting records of the evolving stress field, and developed during the active rise of the Tolfa Dome. On the other hand, meso-scale faults, which are well-clustered, did not record the overall evolution of the stress field.

We here propose that hydrolytic alteration promoted the formation of a well-developed mineralogical zoning, characterized by specific mineral assemblages and petrophysical properties that led to the mechanical compartmentalization of the lithocap. The study of structural, mineralogical, mechanical and hydraulic heterogeneities in lithocaps is thus of paramount importance to study hydraulic connectivity of faults during geothermal energy exploitation.

We finally conclude that a multidisciplinary approach is crucial to study the tectonic evolution of similar fossil hydrothermal systems.

CRediT authorship contribution statement

Barbara Marchesini: Conceptualization, Data curation, Formal analysis, Funding acquisition, Investigation, Methodology, Project administration, Validation, Visualization, Writing – original draft, Writing – review & editing. **Stefano Tavani:** Conceptualization, Data curation, Formal analysis, Investigation, Methodology, Validation, Writing – original draft, Writing – review & editing. **Marco Mercuri:** Data curation, Formal analysis, Investigation, Methodology, Validation, Writing – original draft, Writing – review & editing. **Nicola Mondillo:** Conceptualization, Data curation, Formal analysis, Funding acquisition, Investigation, Methodology, Validation, Writing – original draft, Writing – review & editing. **Mattia Pizzati:** Investigation, Writing – original draft, Writing – review & editing, Methodology, Validation. **Fabrizio Balsamo:** Data curation, Investigation, Methodology, Validation, Writing – original draft, Writing – review & editing. **Luca Aldega:** Data curation, Formal analysis, Investigation, Methodology, Writing – original draft, Writing – review & editing, Funding acquisition. **Eugenio Carminati:** Conceptualization, Funding acquisition, Resources, Validation, Writing – original draft, Writing – review & editing.

Declaration of competing interest

The authors declare that they have no known competing financial interests or personal relationships that could have appeared to influence the work reported in this paper.

Data availability

Data will be made available on request.

Acknowledgements

This work has been funded by the Progetti di Ateneo Sapienza 2021; 2022 to B. Marchesini, 2020 to L. Aldega, 2021 to E. Carminati, 2020; 2022 to M. Mercuri and by the research funds of the Mineral Deposits Studies Group at the Università degli Studi di Napoli Federico II to N. Mondillo. This study was also carried out within the RETURN Extended Partnership and received funding from the European Union Next-GenerationEU (National Recovery and Resilience Plan – NRRP, Mission 4, Component 2, Investment 1.3 – D.D. 1243 August 2, 2022, PE0000005). Giulia Schirripa Spagnolo is thanked for help during field work. Silvia Cattò is thanked for thin section preparations. The careful editorial handling by F. Agosta and constructive comments from two anonymous reviewers helped to improve the manuscript.

Appendix A. Supplementary data

Supplementary data to this article can be found online at https://doi.org/10.1016/j.jsg.2023.105035.

References

Acocella, V., Funiciello, R., 2006. Transverse systems along the extensional Tyrrhenian margin of central Italy and their influence on volcanism. Tectonics 25 (2).

Acocella, V., Rossetti, F., 2002. The role of extensional tectonics at different crustal levels on granite ascent and emplacement: an example from Tuscany (Italy). Tectonophysics 354 (1–2), 71–83.

Agostini, S., Corti, G., Doglioni, C., Carminati, E., Innocenti, F., Tonarini, S., et al., 2006. Tectonic and magmatic evolution of the active volcanic front in El Salvador: insight into the Berlín and Ahuachapán geothermal areas. Geothermics 35 (4), 368–408.

Aldega, L., Cuadros, J., Laurora, A., Rossi, A., 2009. Weathering of phlogopite to beidellite in a karstic environment. Am. J. Sci. 309, 689–710.
Amanda, F.F., Tsuchiya, N., Alviani, V.N., Uno, M., Yamada, R., Shimizu, S., Oyanagi, R., 2022. High-temperature silicified zones as potential caprocks of supercritical geothermal reservoirs. Geothermics 105, 102475.
Bai, T., Maerten, L., Gross, M.R., Aydin, A., 2002. Orthogonal cross joints: do they imply a regional stress rotation? J. Struct. Geol. 24, 77–88.
Balsamo, F., Bezerra, F.H.R., Vieira, M.M., Storti, F., 2013. Structural control on the formation of iron-oxide concretions and Liesegang bands in faulted, poorly lithified Cenozoic sandstones of the Paraíba Basin, Brazil. Bulletin 125 (5–6), 913–931.
Barberi, F., Innocenti, F., Landi, P., Rossi, U., Saitta, M., Santacroce, R.V.I.M., Villa, I.M., 1984. The evolution of Latera caldera (central Italy) in the light of subsurface data. Bull. Volcanol. 47, 125–141.
Barberi, F., Buonasorte, G., Cioni, R., Fiordelisi, A., Foresi, L.M., Iaccarino, S., et al., 1994. Plio-Pleistocene geological evolution of the geothermal area of Tuscany and Latium. Mem. Descr.lla Carta Geol. Italia 49, 77–134.
Barbier, E., 2002. Geothermal energy technology and current status: an overview. Sustainable Energy Reviews 6.
Batini, F., Brogi, A., Lazzarotto, A., Liotta, D., Pandeli, E., 2003. Geological features of Larderello-Travale and Mt. Amiata geothermal areas (southern Tuscany, Italy). Episodes Journal of International Geoscience 26 (3), 239–244.
Brogi, A., 2008. The structure of the Monte Amiata volcano-geothermal area (Northern Apennines, Italy): neogene-Quaternary compression versus extension. Int. J. Earth Sci. 97, 677–703.
Brogi, A., Lazzarotto, A., Liotta, D., Ranalli, G., CROP18 Working Group., 2005. Crustal structures in the geothermal areas of southern Tuscany (Italy): insights from the CROP 18 deep seismic reflection lines. J. Volcanol. Geoth. Res. 148 (1–2), 60–80.
Brogi, A., Fabbrini, L., Liotta, D., 2011. Sb–Hg ore deposit distribution controlled by brittle structures: the case of the Selvena mining district (Monte Amiata, Tuscany, Italy). Ore Geol. Rev. 41 (1), 35–48.
Brogi, A., Liotta, D., Ruggieri, G., Capezzuoli, E., Meccheri, M., Dini, A., 2016. An overview on the characteristics of geothermal carbonate reservoirs in southern Tuscany. Italian Journal of Geosciences 135 (1), 17–29.
Browne, P.R.L., 1978. Hydrothermal alteration in active geothermal fields. Annu. Rev. Earth Planet Sci. 6 (1), 229–248.
Caine, J.S., Evans, J.P., Forster, C.B., 1996. Fault zone architecture and permeability structure. Geology 24 (11), 1025–1028.
Carapezza, M.L., Ranaldi, M., Gattuso, A., Pagliuca, N.M., Tarchini, L., 2015. The sealing capacity of the cap rock above the Torre Alfina geothermal reservoir (Central Italy) revealed by soil CO2 flux investigations. J. Volcanol. Geoth. Res. 291, 25–34.
Carminati, E., Doglioni, C., 2012. Alps vs. Apennines: the paradigm of a tectonically asymmetric Earth. Earth Sci. Rev. 112 (1–2), 67–96.
Cataldi, R., Ferrara, G.C., Stefani, G., Tongiorgi, E., 1969. Contribution to the knowledge of the geothermal field of larderello (Tuscany-Italy). Remarks on the carboli area. Bull. Volcanol. 33, 29–55.
Cataldi, R., Lazzarotto, A., Muffler, P., Squarci, P., Stefani, G., 1978. Assessment of geothermal potential of central and southern Tuscany. Geothermics 7 (2–4), 91–131.
Cavinato, G.P., Celles, P.D., 1999. Extensional basins in the tectonically bimodal central Apennines fold-thrust belt, Italy: response to corner flow above a subducting slab in retrograde motion. Geology 27 (10), 955–958.
Cerrina Feroni, A., Ottria, G., Ellero, A., 2004. The Northern Apennine, Italy: geological structure and transpressive evolution. Florence-2004, 32. Special Volume of The Italian Geological Society For The Igc.
Chiarabba, C., Amato, A., Fiordelisi, A., 1995. Upper crustal tomographic images of the Amiata–Vulsini geothermal region, central Italy. J. Geophys. Res. 100, 4053–4066.
Chiodini, G., Baldini, A., Barberi, F., Carapezza, M.L., Cardellini, C., Frondini, F., et al., 2007. Carbon dioxide degassing at Latera caldera (Italy): evidence of geothermal reservoir and evaluation of its potential energy. J. Geophys. Res. Solid Earth 112 (B12).
Cimarelli, C., De Rita, D., 2006. Relatively rapid emplacement of dome-forming magma inferred from strain analyses: the case of the acid Latian dome complexes (Central Italy). J. Volcanol. Geoth. Res. 158 (1–2), 106–116.
Cinti, D., Procesi, M., Tassi, F., Montegrossi, G., Sciarra, A., Vaselli, O., Quattrocchi, F., 2011. Fluid geochemistry and geothermometry in the western sector of the Sabatini volcanic district and the Tolfa Mountains (Central Italy). Chem. Geol. 284 (1–2), 160–181.
Collettini, C., De Paola, N., Holdsworth, R.E., Barchi, M.R., 2006. The development and behaviour of low-angle normal faults during Cenozoic asymmetric extension in the Northern Apennines, Italy. J. Struct. Geol. 28 (2), 333–352.
Conte, A., Della Ventura, G., Rondeau, B., Romani, M., Cestelli Guidi, M., La, C., et al., 2022. Hydrothermal genesis and growth of the banded agates from the Allumiere-Tolfa volcanic district (Latium, Italy). Phys. Chem. Miner. 49 (10), 39.
Conti, P., Cornamusini, G., Carmignani, L., 2020. An outline of the geology of the Northern Apennines (Italy), with geological map at 1: 250,000 scale. Italian Journal of Geosciences 139 (2), 149–194.
Corrado, S., Aldega, L., Celano, A.S., De Benedetti, A.A., Giordano, G., 2014. Cap rock efficiency and fluid circulation of natural hydrothermal systems by means of XRD on clay minerals (Sutri, Northern Latium, Italy). Geothermics 50, 180–188.
Curzi, M., Caracausi, A., Rossetti, F., Rabiee, A., Billi, A., Carminati, E., Aldega, L., Bernasconi, S.M., Boschi, C., Drivenes, K., Rizzo, A.L., Sørensen, B.E., 2022. From fossil to active hydrothermal outflow in the back-arc of the central Apennines (Zannone Island, Italy). G-cubed 23, e2022GC010474.
de Rita, D., Bertagnini, A., Faccenna, C., Landi, P., Rosa, C., Zarlenga, F., Di Filippo, M., Carboni, M.G., 1997. Evoluzione geopetrografica-strutturale dell'area tolfetana. Boll. Soc. Geol. Ital. 116 (1), 143–175.
Destro, N., 1995. Release fault: a variety of cross fault in linked extensional fault systems, in the Sergipe-Alagoas Basin, NE Brazil. J. Struct. Geol. 17, 615–629.
Dini, A., Westerman, D.S., Innocenti, F., Rocchi, S., 2008. Magma emplacement in a transfer zone: the Miocene mafic Orano dyke swarm of Elba Island, Tuscany, Italy. Geological Society, London, Special Publications 302 (1), 131–148.
Doveri, M., Lelli, M., Marini, L., Raco, B., 2010. Revision, calibration, and application of the volume method to evaluate the geothermal potential of some recent volcanic areas of Latium, Italy. Geothermics 39 (3), 260–269.
Duchi, V., Minissale, A., Paolieri, M., Prati, F., Valori, A., 1992. Chemical relationship between discharging fluids in the Siena-Radicofani graben and the deep fluids produced by the geothermal fields of Mt Amiata, Torre Alfina and Latera (Central Italy). Geothermics 21 (3), 401–413.
Ece, O.I., Schroeder, P.A., 2007. Clay mineralogy and chemistry of halloysite and alunite deposits in the Turplu area, Balikesir, Turkey. Clay Clay Miner. 55 (1), 18–35.
Ece, Ö.I., Ekinci, B., Schroeder, P.A., Crowe, D., Esenli, F., 2013. Origin of the Düvertepe kaolin–alunite deposits in Simav Graben, Turkey: timing and styles of hydrothermal mineralization. J. Volcanol. Geoth. Res. 255, 57–78.
Engelder, T., 1987. Joints and shear fractures in rock. Fracture mechanics of rock 2, 27–69.
Erkan, K., Holdmann, G., Benoit, W., Blackwell, D., 2008. Understanding the Chena Hot Springs, Alaska, geothermal system using temperature and pressure data from exploration boreholes. Geothermics 37 (6), 565–585.
Faccenda, M., Minelli, G., Gerya, T.V., 2009. Coupled and decoupled regimes of continental collision: Numerical modeling. Earth Planet. Sci. Lett. 278 (3–4), 337–349.
Fazzini, P., Mp, M., 1972. Geologia dei Monti della Tolfa (Lazio settentrionale; province di Viterbo e Roma.
Ferrill, D.A., Smart, K.J., Cawood, A.J., Morris, A.P., 2021. The fold-thrust belt stress cycle: superposition of normal, strike-slip, and thrust faulting deforma- tion regimes. J. Struct. Geol. 148, 104362.
Funiciello, R., Rita, D.D., Sposato, A., Esposito, A., Fabbri, M., Marsili, P., Trigari, A., 2012. Note illustrative della Carta Geologica d'Italia alla scala 1: 50.000-foglio 354 Tarquinia. Presidenza del Consiglio dei Ministri, *Agenzia per la Protezione dell'Ambiente e per i servizi Tecnici: Roma, Italy, Servizio Geologico d'Italia, scale*, 1 (50,000).
Ganguly, S., Mohan Kumar, M.S., 2012. Geothermal reservoirs—a brief review. J. Geol. Soc. India 79, 589–602.
Gianelli, G., Manzella, A., Puxeddu, M., 1997. Crustal models of the geothermal areas of southern Tuscany (Italy). Tectonophysics 281 (3–4), 221–239.
Giordano, G., Ahumada, M.F., Aldega, L., Baez, W.A., Becchio, R.A., Bigi, S., et al., 2016. Preliminary Data on the Structure and Potential of the Tocomar Geothermal Field (Puna Plateau, Argentina).
González-Partida, E., Camprubí, A., López-Hernández, A., Santoyo, E., Izquierdo-Montalvo, G., Pandarinath, K., et al., 2022. Distribution of hypogene alteration and fluid evolution in the Los Humeros Geothermal Field (Puebla, Mexico): multiple sourced fluids, interrelations, and processes in a superhot system. Appl. Geochem. 136, 105159.
Gross, M.R., 1993. The origin and spacing of cross joints: examples from the Monterey Formation, Santa Barbara Coastline, California. J. Struct. Geol. 15, 737–751.
Hedenquist, J.W., Arribas, A., 2022. Exploration implications of multiple formation environments of advanced argillic minerals. Econ. Geol. 117 (3), 609–643.
Hedenquist, J.W., Arribas, Gonzalez-Urien, E., 2000. Exploration for epithermal gold deposits. In: Gold in 2000, SEG Reviews, vol. 13, pp. 245–277.
Hemley, J.J., Jones, W.R., 1964. Chemical aspects of hydrothermal alteration with emphasis on hydrogen metasomatism. Econ. Geol. 59 (4), 538–569.
Hu, Z., Zhang, Y., Zeng, Y., 2023. Controlling Effects of Cap Rocks on the Formation of Deep Geothermal Resources. Energy Geoscience, 100208.
Jolivet, L., Faccenna, C., D'Agostino, N., Fournier, M., Worrall, D., 1999. The kinematics of back-arc basins, examples from the Tyrrhenian, Aegean and Japan Seas. Geological Society, London, Special Publications 164 (1), 21–53.
Krupp, R.E., Seward, T.M., 1987. The Rotokawa geothermal system, New Zealand; an active epithermal gold-depositing environment. Econ. Geol. 82 (5), 1109–1129.
Liotta, D., Brogi, A., Meccheri, M., Dini, A., Bianco, C., Ruggieri, G., 2015. Coexistence of low-angle normal and high-angle strike-to oblique-slip faults during Late Miocene mineralization in eastern Elba Island (Italy). Tectonophysics 660, 17–34.
Liotta, D., Brogi, A., Ruggieri, G., Zucchi, M., 2021. Fossil vs. active geothermal systems: a field and laboratory method to disclose the relationships between geothermal fluid flow and geological structures at depth. Energies 14 (4), 933.
Luhmann, A.J., Tutolo, B.M., Bagley, B.C., Mildner, D.F., Seyfried Jr., W.E., Saar, M.O., 2017. Permeability, porosity, and mineral surface area changes in basalt cores induced by reactive transport of CO 2-rich brine. Water Resour. Res. 53 (3), 1908–1927.
Luo, J., Hu, R., Shi, S., 2015. Timing of uranium mineralization and geological implications of Shazijiang granite-hosted uranium deposit in Guangxi, South China: new constraint from chemical U-Pb age. J. Earth Sci. 26, 911–919.
Macente, A., Vanorio, T., Miller, K.J., Fusseis, F., Ogawa, T., Ishikawa, T., et al., 2017. Geochemical anomaly in ancient subduction boundary fault: trench-parallel heterogeneity in slip behavior caused by variation of mineral composition. AGU Fall Meeting Abstracts 2017, H43G–H1721.
Maerten, F., Maerten, L., Plateaux, R., Cornard, P.H., 2022. Joint inversion of tectonic stress and magma pressures using dyke trajectories. Geol. Mag. 159 (11–12), 2379–2394.
Maffucci, R., Corrado, S., Aldega, L., Bigi, S., Chiodi, A., Di Paolo, L., Giordano, G., Invernizzi, C., 2016. Cap rock efficiency of geothermal systems in fold-and-thrust belts: evidence from paleo-thermal and structural analyses in Rosario de La Frontera geothermal area (NW Argentina). J. Volcanol. Geoth. Res. 328, 84–95.

Marchesini, B., Carminati, E., Aldega, L., Mirabella, F., Petrelli, M., Caracausi, A., Barchi, M.R., 2022. Chemical interaction driven by deep fluids in the damage zone of a seismogenic carbonate fault. J. Struct. Geol. 161, 104668.
Marroni, M., Molli, G., Ottria, G., Pandolfi, L., 2001. Tectono-sedimentary evolution of the External Liguride units (Northern Apennines, Italy): insights in the pre-collisional history of a fossil ocean-continent transition zone. Geodin. Acta 14 (5), 307–320.
Masoch, S., Fondriest, M., Gomila, R., Jensen, E., Mitchell, T.M., Cembrano, J., et al., 2022. Along-strike architectural variability of an exhumed crustal-scale seismogenic fault (Bolfin Fault Zone, Atacama Fault System, Chile). J. Struct. Geol. 165, 104745.
Maza, S.N., Collo, G., Morata, D., Taussi, M., Vidal, J., Mattioli, M., Renzulli, A., 2021. Active and fossil hydrothermal zones of the Apacheta volcano: insights for the Cerro Pabellón hidden geothermal system (Northern Chile). Geothermics 96, 102206.
Mège, D., Masson, P., 1996. A plume tectonics model for the Tharsis province, Mars. Planet. Space Sci. 44 (12), 1499–1546.
Moeck, I.S., 2014. Catalog of geothermal play types based on geologic controls. Renew. Sustain. Energy Rev. 37, 867–882.
Negretti, G.C., 1962. Osservazioni vulcanologiche e petrografiche sui tufi caotici e le ignimbriti dei Monti del Sassetto (Tolfa). Rend. Soc. Min. It 19, 171–187.
Peccerillo, A., 2005. Plio-quaternary volcanism in Italy, Vol. 365. Springer-Verlag Berlin Heidelberg, New York.
Pinarelli, L., 1991. Geochemical and isotopic (Sr, Pb) evidence of crust-mantle interaction in acidic melts—the Tolfa-Cerveteri-Manziana volcanic complex (central Italy): a case history. Chem. Geol. 92 (1–3), 177–195.
Quintà, A., Tavani, S., Roca, E., 2012. Fracture pattern analysis as a tool for constraining the interaction between regional and diapir-related stress fields: poza de la Sal Diapir (Basque Pyrenees, Spain). Geological Society, London, Special Publications 363 (1), 521–532.
Ricci Lucchi, F., 1986. The Oligocene to Recent foreland basins of the northern Apennines. Foreland Basins 103–139.
Rossetti, F., Aldega, L., Tecce, F., Balsamo, F., Billi, A., Brilli, M., 2011. Fluid flow within the damage zone of the Boccheggiano extensional fault (Larderello–Travale geothermal field, central Italy): structures, alteration and implications for hydrothermal mineralization in extensional settings. Geol. Mag. 148 (4), 558–579.
Rye, R.O., Bethke, P.M., Wasserman, M.D., 1992. The stable isotope geochemistry of acid sulfate alteration. Econ. Geol. 87 (2), 225–262.
Salinas, P., Regnier, G., Jacquemyn, C., Pain, C.C., Jackson, M.D., 2021. Dynamic mesh optimisation for geothermal reservoir modelling. Geothermics 94, 102089.
Sibson, R.H., 1987. Earthquake rupturing as a mineralizing agent in hydrothermal systems. Geology 15 (8), 701–704.
Sillitoe, R.H., Steele, G.B., Thompson, J.F.H., Lang, J.R., 1998. Advanced argillic lithocaps in the Bolivian tin-silver belt. Miner. Deposita 33, 539–546.
Smeraglia, L., Mercuri, M., Tavani, S., Pignalosa, A., Kettermann, M., Billi, A., Carminati, E., 2021. 3D Discrete Fracture Network (DFN) models of damage zone fluid corridors within a reservoir-scale normal fault in carbonates: multiscale approach using field data and UAV imagery. Mar. Petrol. Geol. 126, 104902.
Smith, S.A., Bistacchi, A., Mitchell, T.M., Mittempergher, S., Di Toro, G., 2013. The structure of an exhumed intraplate seismogenic fault in crystalline basement. Tectonophysics 599, 29–44.
Storti, F., Balsamo, F., Cappanera, F., Tosi, G., 2011. Sub-seismic scale fracture pattern and in situ permeability data in the chalk atop of the Krempe salt ridge at Lägerdorf, NW Germany: inferences on synfolding stress field evolution and its impact on fracture connectivity. Mar. Petrol. Geol. 28 (7), 1315–1332.
Taussi, M., Brogi, A., Liotta, D., Nisi, B., Perrini, M., Vaselli, O., et al., 2022. CO2 and heat energy transport by enhanced fracture permeability in the Monterotondo Marittimo-Sasso Pisano transfer fault system (Larderello Geothermal Field, Italy). Geothermics 105, 102531.
Vázquez, M., Nieto, F., Morata, D., Droguett, B., Carrillo-Rosua, F.J., Morales, S., 2014. Evolution of clay mineral assemblages in the Tinguiririca geothermal field, Andean Cordillera of central Chile: an XRD and HRTEM-AEM study. J. Volcanol. Geoth. Res. 282, 43–59.
Vignaroli, G., Pinton, A., De Benedetti, A.A., Giordano, G., Rossetti, F., Soligo, M., Berardi, G., 2013. Structural compartmentalisation of a geothermal system, the Torre Alfina field (central Italy). Tectonophysics 608, 482–498.
Villa, I.M., Giuliani, O., de Grandis, G., Cioni, R., 1989. Datazioni K–Ar dei vulcani di Tolfa e Manziana. Bollettino GNV 1989/2, 1025–1026.
Williams, J.N., Toy, V.G., Smith, S.A., Boulton, C., 2017. Fracturing, fluid-rock interaction and mineralisation during the seismic cycle along the Alpine Fault. J. Struct. Geol. 103, 151–166.
Wintsch, R.P., Christoffersen, R., Kronenberg, A.K., 1995. Fluid-rock reaction weakening of fault zones. J. Geophys. Res. Solid Earth 100 (B7), 13021–13032.
Yang, K., Browne, P.R.L., Huntington, J.F., Walshe, J.L., 2001. Characterising the hydrothermal alteration of the Broadlands–Ohaaki geothermal system, New Zealand, using short-wave infrared spectroscopy. J. Volcanol. Geoth. Res. 106 (1–2), 53–65.
Zhang, W., Jiménez-Munt, I., Torne, M., Vergés, J., Bravo-Gutiérrez, E., Negredo, A.M., Fernàndez, M., 2022. Geophysical-Petrological Model for Bidirectional Mantle Delamination of the Adria Microplate Beneath the Northern Apennines and Dinarides Orogenic Systems. J. Geophys. Res. Solid Earth 127 (12), e2022JB024800.
Zucchi, M., Brogi, A., Liotta, D., Caggianelli, A., Dini, A., Ventruti, G., et al., 2022. Fractures, fluid flow and inherited structures in geothermal systems: inputs from the Fe-ore deposits of eastern Elba Island (Northern Apennines, Italy). Geol. Mag. 159 (11–12), 2238–2261.